Universidade Estadual de Maringá
Centro de Ciências Exatas
Departamento de Física
Programa de Pós-Graduação em Física

Otávio Augusto Capeloto

Indução e detecção de deformações superficiais em metais e líquidos utilizando as Espectroscopias de Espelho Fototérmico/Fotomecânico

Maringá
2018

Universidade Estadual de Maringá
Centro de Ciências Exatas
Departamento de Física
Programa de Pós-Graduação em Física

Otávio Augusto Capeloto

Induction and detection of surface deformations in metals and liquids using Photothermal Mirror and Photomecanical Mirror Spectroscopies

Maringá
2018

Otávio Augusto Capeloto

Indução e detecção de deformações superficiais em metais e líquidos utilizando as Espectroscopias de Espelho Fototérmico/Fotomecânico

Tese apresentada à Universidade Estadual de Maringá, como requisito parcial para a obtenção do título de doutor em Física.

Orientador: Prof. Dr. Nelson Guilherme Castelli Astrath
Coorientador: Prof. Dr. Gustavo Vinicius Bassi Lukasievicz
Coorientador: Prof. Dr. Tomaž Požar

Maringá
2018

Dados Internacionais de Catalogação-na-Publicação (CIP)
(Biblioteca Central - UEM, Maringá – PR., Brasil)

Capeloto, Otávio Augusto

C238i Indução e detecção de deformações superficiais em metais e líquidos utilizando as espectroscopias de espelho fototérmico/fotomecânico./ Otávio Augusto Capeloto. –- Maringá, 2018.

70 f. : il. color, figs. , tabs.

Orientador: Prof. Dr. Nelson Guilherme Castelli Astrath.
Coorientador: Prof. Dr. Gustavo Vinicius Bassi Lukasievicz.
Coorientador: Prof. Dr. Tomaž Požar.

Tese (doutorado) – Universidade Estadual de Maringá, Centro de Ciências Exatas, Programa de Pós-Graduação em Física, 2018.

1. Deformações superficiais. 2. Fenômenos fototérmicos. 3. Pressão de radiação. 4. Espelho fototérmico. 5. Espelho fotomecânico. 6. Ondas mecânicas. I. Astrath, Nelson Guilherme Castelli, orient. II. Lukasievicz, Gustavo Vinicius Bassi, coorient. III. Požar, Tomaž, coorient. IV. Universidade Estadual de Maringá. Centro de Ciências Exatas. Programa de Pós-Graduação em Física. V. Título.

CDD 22. ED.534.55
Jane Lessa Monção CRB 1173

Otávio Augusto Capeloto

Induction and detection of surface deformations in metals and liquids using Photothermal Mirror and Photomecanical Mirror Spectroscopies

Thesis presented to the State University of Maringá, in partial fulfillment of the requirements for the degree of Doctor of Science (Physics).

Advisor: Prof. Dr. Nelson Guilherme Castelli Astrath
Co-advisor: Prof. Dr. Gustavo Vinicius Bassi Lukasievicz
Co-advisor: Prof. Dr. Tomaž Požar

Maringá
2018

OTÁVIO AUGUSTO CAPELOTO

INDUÇÃO E DETECÇÃO DE DEFORMAÇÕES SUPERFICIAIS EM METAIS E LÍQUIDOS UTILIZANDO AS ESPECTROSCOPIAS DE ESPELHO FOTOTÉRMICO/FOTOMECÂNICO

Tese apresentada à Universidade Estadual de Maringá, como requisito parcial para a obtenção do título de doutor.

Aprovado em: Maringá, 01 de outubro 2018.

BANCA EXAMINADORA

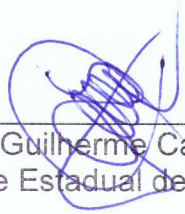

Prof. Dr. Nelson Guilherme Castelli Astrath
Universidade Estadual de Maringá

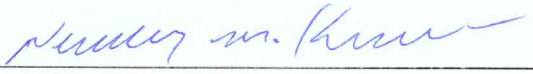

Prof. Dr. Newller Marcelo Kimura
Universidade Estadual de Maringá

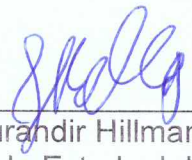

Prof. Dr. Jurandir Hillmann Rohling
Universidade Estadual de Maringá

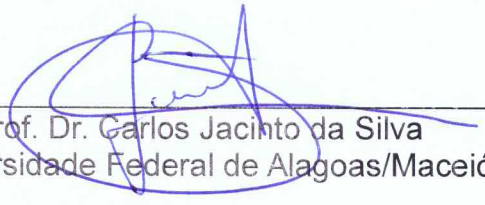

Prof. Dr. Carlos Jacinto da Silva
Universidade Federal de Alagoas/Maceió

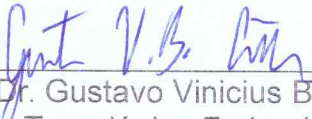

Prof. Dr. Gustavo Vinicius Bassi Lukasievicz
Universidade Tecnológica Federal do Paraná/Medianeira

Agradecimentos

Gostaria de agradecer a todas as pessoas que direta ou indiretamente contribuíram para a realização deste trabalho:

Ao meu pai Antonio Capeloto e a minha Mãe Elisa R. B. Capeloto pelo apoio em meus estudos e em todas a lições dadas em minha vida. Aos meus irmãos Débora C. Capeloto e Ulisses R. Capeloto pelo grande incentivo dado em todos os momentos.

A minha esposa, Marilaini Vizioli de Castro, pelo apoio, compreensão, paciência e incentivo em todos os momentos.

A minha segunda família, Lucileni Vizioli, Cristiane Vizioli, Lidiane Vizioli, Eduardo Ghizoni e Henrique Hoshino por todo o apoio e incentivo.

Ao professor Dr. Nelson Guilherme Castelli Astrath pela orientação e incentivo neste trabalho.

Ao Prof. Dr. Gustavo Vinicius Bassi Lukasievicz pela coorientação e incentivo e ajuda neste trabalho.

Ao Prof. Dr. Tomaž Požar por todas as explicações, coorientação e ajuda em fases importantes do trabalho.

Ao professor Dr. Luis Carlos Malacarne pela ajuda e explicação em muitas dúvidas.

Ao Dr. Vitor Santaella Zanuto pela contribuição importante no trabalho, por outras ajudas e por conversas aleatórias nos cafés do dia a dia.

Aos amigos: Elton, Pablo, Patrick, Marcelo, Raquel Bini, Rafa, "Andershow" Gonçalvez, Gabriel Meninão, Vinicius Granatto, Robson Muniz, Thiago Moreno, Thiago Petrucci, Renan Biagio, Veridiana Guimarães, Maike, pelas conversas e discussões.

Aos professores, Dr. Antonio Medina Neto, Dra. Francielle Sato, Dr. Antonio Carlos Bento e Dr. Mauro Luciano Baesso.

Aos funcionários do Departamento de Física, em especial, Jurandir, Márcio, Marcos, Mônica, Zelito, Sérgio e Adriano.

As agências que financiaram este projeto, Capes, CNPq, Fundação Araucária.

Resumo

Os métodos fototérmicos são ferramentas muito sensíveis para a caracterização de efeitos localizados induzidos por laser em materiais. Neste trabalho, a técnica de espelho fototérmico é usada para investigar ondas termoelásticas geradas por deposição localizada de calor. A excitação por laser pulsado é usada para gerar perturbações mecânicas em metais. Essa técnica detecta a distorção da frente de onda do feixe de prova refletido na superfície da amostra perturbada. Deformação na escala nanométrica é induzida sob a superfície iluminada, e ondas termoelásticas transientes de menor amplitude propagam-se na superfície. Os resultados numéricos e experimentais mostram boa concordância e representam a deformação de longa duração devido à difusão térmica e as ondas induzidas devido à rápida perturbação. Em um aparato experimental similar, o método de espelho fotomecânico é usado para induzir deformações superficiais em escalas nanométricas explorando a conservação de momento na interação entre líquidos dielétricos e um feixe laser. O efeito de força de radiação na interface ar/líquido é quantitativamente avaliado para fluidos com diferentes densidades, viscosidades e tensões superficiais. A pressão aplicada nos líquidos por laser contínuo ou pulsado é totalmente descrita pela densidade de força eletromagnética de Helmholtz.

Abstract

Photothermal methods are powerful tools for characterizing laser induced localized effects in materials. Here we use the photothermal mirror method to investigate the thermoelastic waves launched by a localized heat deposition. Pulsed laser excitation is used to generate mechanical perturbations in metals. This method detects the wavefront distortion of the probe beam reflected from the perturbed sample surface. Nanometer scale expansion of the material is induced just under the irradiated surface releasing transient thermoelastic waves of much smaller amplitudes on the surface. Numerical predictions and the experimental results are in a good agreement and represent both the thermal diffusion of the large amplitude, long-lasting outward bulge and the released elastic waves. Using a slightly different experimental approach, the photomechanical mirror method is used to induce nanometer-scale surface deformation by exploiting momentum conservation of the interaction between laser light and dielectric liquids. The effect of radiation force at the air-liquid interface is quantitatively assessed for fluids with different density, viscosity and surface tension. The imparted pressure on the liquids by continuous or pulsed laser light excitation is fully described by the Helmholtz electromagnetic force density.

Symbol List

α_T [10^{-6} 1/K] Linear thermal expansion coefficient;

β_{f} [m^{-1}] Absorption coefficient of fluid;

β_{s} [m^{-1}] Absorption coefficient of sample;

δ Dirac's delta;

δ_{ij} Kronecker's delta;

γ [N/m] Surface tension;

ϵ_{ij} Strain tensor;

ε [F/m] Electric permittivity of material;

ε_0 [F/m] Electric permittivity of vacuum;

ε_{r} Relative electric permittivity;

λ [Pa] 1st Lamè constant;

λ_{p} [m] Probe beam wavelength;

μ [Pa·s][1] Dinamic viscosity;

μ_0 [H/m] Magnetic permeability of vacuum;

μ_{l} [Pa] 2nd Lamè constant;

μ_{m} [H/m] Magnetic permeability of material;

[1] In Chapter 3 the unit used is cP=mPa·s

μ_{r} Relative magnetic permeability;

ν Poisson's ratio;

ξ_{p} [s] Time of maximum irradiance of pulse;

ρ [kg/m^3] Mass density; (Chapter 3 and Appendix A)

ρ_{f} [kg/m^3] Mass density of fluid; (Chapter 2)

ρ_{s} [kg/m^3] Mass density of sample; (Chapter 2)

σ_{ij} [Pa] Stress tensor;

τ_{p} [s] Pulse width;

ϕ Rate of luminous energy converted into heat;

ω_{e} [m] Excitation beam radius at sample surface;

$\omega_{0\mathrm{p}}$ [m] Probe beam radius at waist;

$\omega_{1\mathrm{p}}$ [m] Probe beam radius at sample surface;

$\vec{B}$ [T] Magnetic flux density;

c [m/s] Speed of light in vacuum;

c_{H} [m/s] Velocity of Head waves;

c_{P} [m/s] Velocity of Primary waves;

c_{R} [m/s] Velocity of Rayleigh waves;

c_{S} [m/s] Velocity of Secondary waves;

$C_{p\mathrm{f}}$ [J/(kg· K)] Specific Heat of fluid;

$C_{p\mathrm{s}}$ [J/(kg· K)] Specific Heat of sample;

$\vec{D}$ [C/m^2]Electric Displacement field;

$D_{T\mathrm{f}}$ [m^2/s] Thermal diffusivity of fluid;

$D_{T\mathrm{s}}$ [m^2/s] Thermal diffusivity of sample;

E_{n} [J] Energy of pulsed excitation laser beam;

$\vec{E}$ [V/m] Electric field;

E_{inc} [V/m] Incident electric field;

$\vec{F}$ [N] Volume force;

$\vec{g}$ [m/s^2] Acceleration of gravity;

$\vec{H}$ [A/m]Magnetic field;

k_{f} [W/(m $\cdot$ K)] Thermal conductivity of fluid;

k_{s} [W/(m $\cdot$ K)] Thermal conductivity of sample;

n Refractive index;

$p(\vec{r})$ [Pa] Pressure;

p_0 [kg·m/s] Linear momentum of light in vacuum;

p_{A} [kg·m/s] Abraham momentum of light;

p_{M} [kg·m/s] Minkowski momentum of light;

P_{e} [W] Power of cw excitation laser beam;

R_{s} Reflectance of sample;

$\vec{u}$ [m] Displacement;

U [J] Energy of light;

$z_{1\mathrm{e}}$ [m] Distance between the sample surface and excitation beam waist;

$z_{1\mathrm{p}}$ [m] Distance between the sample surface and probe beam waist;

$z_{2\mathrm{p}}$ [m] Distance between the sample surface and the photodetector;

z_{ce} [m] Excitation beam confocal distance;

z_{cp} [m] Probe beam confocal distance;

Y [Pa] Young's modulus;

Contents

Chapter 1

Introduction

The interaction between light and matter may generate elastic waves by heating the material (thermoelastic effect, an energy transfer dominated effect) or by the momentum exchange between light and matter (radiation pressure, a momentum transfer dominated effect) [1]. In the former, energy related effect, part of the energy is absorbed in the material and then converted into heat [2–4]. The rapid deposition of light energy acts as a source of mechanical waves in the material. The induced thermal expansion launches various types of mechanical disturbances [5–9]. Within the bulk of the material, longitudinal (P-waves) and shear waves (S-waves) radiate spherically away from the source. They are accompanied by the surface-bound Rayleigh waves (R-waves) and the Mach-cone shaped head waves (H-waves) [2, 3]. A representation of these types of waves is shown in Fig. 1.1. At high power density levels, ablation effect may occur in solids modifying the state of the surface. Below the ablation threshold, at moderate power densities, thermoelastic waves dominate over radiation pressure induced waves in solids [10].

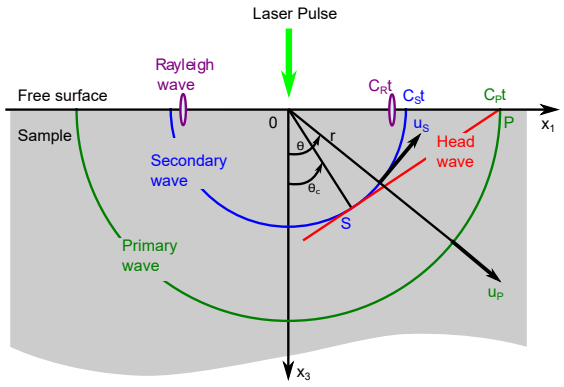

Figure 1.1: Volumetric and surface waves generated in a sample at thermoelastic regime by a pulsed laser [2]. u_p stands for displacement of particles due to the Primary wave, u_s stands for displacement of particles due to the Secondary wave. c_P is the velocity of the Primary wave, c_S the velocity of the Secondary wave, c_R the velocity of the Rayleigh wave, and θ_c is the critical angle. x_1 is the radial axis and x_3 is the azimutal axis.

Momentum transfer from light to matter always generates elastic waves in deformable media. The correct mathematical expression for the momentum of light within

dielectric materials and the effects caused by the radiation forces when light passes through adjacent media have been extensively debated for over a century [11–19]. The effects of radiation pressure exerted on a dielectric surface exposed to electromagnetic radiation can be interpreted as the transfer of momentum from electromagnetic field at the surface normal of the incident electromagnetic radiation. Although the momentum-driven elastic waves are predicted by electrodynamic and the elastodynamic theories, the temporal evolution of the displacement field generated in this process has yet to be precisely measured.

Detection of light-induced elastic waves is feasible with many different experimental approaches [2,3,5–10,20–24]. Bulk and surface waves can be detected utilizing capacitive, piezoelectric, electromagnetic and optical transduction mechanisms [25]. The possibility of remote generation and stand-off detection of elastic waves using optical probes makes photothermal methods attractive for material characterization [20] and non-destructive testing [2–4]. For instance, a number of pump-probe methods have been employed to detect mechanical perturbations in solids using either interferometric schemes, photothermal beam deflection or by analyzing diffraction wavefront distortions. As opposed to the capacitive, electromagnetic or piezoelectric sensors, the above-mentioned optical methods can be used to detect elastic waves created just underneath the pulse excitation area [9, 20, 26, 27]. The ability of probing the region of the largest temperature variation and mechanical deformation makes them an attractive complementary approach.

One of the optical approaches to detect elastic waves is also the photothermal/ photomechanical mirror (PTM) technique. Here, the mechanical surface displacement are detected by analyzing the focusing or defocusing of the probe beam reflected from the sample surface in the far field region [21, 22, 24, 28]. This method has been recently introduced under pulsed Gaussian laser excitations for the measurement of thermal diffusivity and thermo-optical properties of semi-transparent and opaque solids [22, 23]. Using a slightly different experimental approach, this method has also been proved capable of measuring the surface deformation induced by radiation pressure at air-liquid interface induced by continuous and pulsed laser excitation [28].

The complex nature of elastic waves has brought the current development of photothermal/photomechanical methods, with concurrent interferometric detection schemes, to a breakthrough stage where nano- and sub-nanometer-scale deformations can be detected with highly detailed spatial and temporal resolutions [28]. The advances recently made in the development of the photothermal/photomechanical methods have opened a new pathway to look into the localized effects created by laser excitation. Here we give a detailed description of two different applications of the photothermal/photomechanical method to investigate photo-induced elastic waves generated by either heating opaque metals (thermoelastic effect) or by the momentum transfer from light to liquids (radiation pressure).

In Chapter 2, we show that pulsed laser excitation in metals launches elastic waves that propagate on the surface and within the solids generating convoluted photothermal mirror signals following the thermo-mechanical properties of the sample. The elastic waves are predicted by numerical solution of the thermoelastic equation and have properties closely related to the familiar elastic waves created by an isotropic point-expansion source on the surface of solids.

In Chapter 3, we induce nanometer-scale surface deformation by exploiting momentum conservation of the interaction between laser light and dielectric liquids. The effect of radiation force at the air-liquid interface is quantitatively assessed for fluids with different density, viscosity and surface tension. The imparted pressure on the liquids by continuous or pulsed laser light excitation is fully described by the Helmholtz electromagnetic force density. It is our belief that the novel pump-probe experimental methods we have been developing, in addition to first-principle numerical modeling, are at the edge of answering the question of what formalism of the classical theory of electromagnetism correctly describes the effects of momentum transfer between light and matter.

Chapter 2

Generation and detection of thermoelastic waves in metals by a photothermal mirror method[1]

In this chapter, we present an investigation of the thermoelastic waves launched by a localized heat deposition in metals. Pulsed laser excitation is used to generate mechanical perturbations in metals that are detected using the photothermal mirror method. This method detects the wavefront distortion of the probe beam reflected from the perturbed sample surface. Nanometer scale expansion of the material is induced just under the irradiated surface releasing transient thermoelastic waves of much smaller amplitudes on the surface. Numerical predictions and the experimental results are in a good agreement and represent both the thermal diffusion of the large amplitude, long-lasting outward bulge and the released elastic waves.

2.1 Introduction

The study of the propagation of mechanical waves in a given material is of great interest. It originates and has been extensively investigated in seismology [29]. Seismological applications vary from exploration for minerals, oil, natural gas, to the development

[1]This chapter is partially reproduced from Capeloto, O. A. et al. "Generation and detection of thermoelastic waves in metals by a photothermal mirror method." Applied Physics Letters **109**, 191908 (2016); doi: 10.1063/1.4967530, with the permission of AIP Publishing. The authorization letter is indexed in Appendix A.1.

of earthquake resistant constructions. Seismology had its great advance in 1880 when methods of detection (seismographs) and methods of mathematical physics began to be applied to the understanding of the waves generated in an earthquake. The concepts of mechanical waves involved in seismology can be applied in non-destructive methods to obtain mechanical parameters in materials and also in image diagnostics [29].

The description of mechanical waves propagating in a medium is well established by the theory of elasticity. Considerable theoretical advances in this field were made by Navier, Poisson, Rayleigh and Lamb [29–32]. In 1821 Navier introduced, from the concepts of Hooke's law, an equation of equilibrium and vibrations for an elastic body. In 1831, Poisson obtained theoretically the concept for two types of waves, the longitudinal and shear waves [30], also known as P and S waves, respectively. Rayleigh [31], in 1887 theoretically described waves propagating on the surface of an elastic material. Lamb [32], in 1903, showed the first theoretical seismogram for a point source buried in the middle of a homogeneous semi-space.

First theoretical works treating thermally induced waves in solids are attributed to Danilovskaya [33, 34], Michels [35] and Boley [36]. White [37] in 1963 was one of the pioneers in the induction and detection of elastic waves in metals caused by electron bombardment and radio-frequency absorption on the surface of a body. The amplitude of generated waves was correlated to the characteristics of the input flux and the thermal and elastic properties of the body. Wave detection was performed using a barium titanate crystal, which has piezoelectric properties. Scruby *et al.* [38] in 1980 showed the generation of elastic waves via laser. In this method, the waves are induced by thermal expansion of a metal heated by laser. A transducer was used for detection, and the observation of the waves was performed on the surface opposite to the illuminated one. It was considered that the source of thermoelastic waves could be due to the dipole forces acting on the material. In 1984, Rose [39] developed the theoretical background assuming the thermoelastic source as a point source. A general representation in terms of Green's functions was used, as described for volumetric sources by Aki and Richards [29]. Aki and Richards represent the Green's functions as the solution to the equation [29]

$$\rho_{\mathrm{s}}\frac{\partial^2}{\partial t^2}G_{in} = \delta_{in}\delta(\vec{x}-\vec{\xi})\delta(t-\tau) + \frac{\partial}{\partial x_j}\left(c_{ijkl}\frac{\partial G_{kn}}{\partial x_j}\right), \tag{2.1}$$

where

$$c_{ijkl} = \mu_{\mathrm{l}}[(1-2\nu)^{-1}2\nu\delta_{ij}\delta_{kl} + \delta_{ik}\delta_{jl} + \delta_{il}\delta_{jk}] \tag{2.2}$$

for isotropic materials. ρ_{s} is the mass density of the material, μ_{l} the Lame's constant, and ν the Poisson's ratio. However, Rose [39] used a Heaviside function $H(t)$ instead a Dirac Delta function in time, $\delta(t)$. In Rose's model, the direct derivation of the temperature variation in a sample using the heat diffusion equation is not necessary, since the source

term that the heat conduction equation carries is implicitly attributed to the strength of the point source, or seismic moment [39], that is related to the source strength and characterizes all the information about the source [29] . Displacement expressions for different positions were obtained. In that context, the point source representation together with a Heaviside function in time became a good approximation for comparisons with experiments. This is because the Heaviside function allows the displacement in far field to be written as a function of the arrival times of the longitudinal and transverse waves. However, this model may render different results when compared to a finite-source term because the z-coordinate stress components do not completely cancel each other [38]. In 1989, McDonald [7], obtained mathematical simplifications of Rose's model by considering a hyperbolic heat diffusion equation [7], assuming the thermal propagation velocity finite and equal to the velocity of the longitudinal waves. Thus, the problem was translated to generalized thermoelasticity theory rather than to the classical theory [40]. However, the wave term in the temperature expression does not significantly affect the results when compared to that found by Rose previously. This means that Rose's solution for a buried point source is a reasonably good model for a transient thermoelastic source, often encountered by laser absorption in the nanosecond pulse duration range.

Although piezoelectric and capacitive methods are known for their high sensitivity, pump-probe detection of laser induced elastic waves has advantages for material characterization [5]. The remote nature of optical detection allows for measurements to be performed at high and low temperatures and the simultaneous detection of volume and surface waves [5]. Using the methods, such as with interferometric, deflection or wavefront distortion analysis, it is possible to prove the effect just underneath the illuminated area, where maximum displacements are produced [9, 20, 26, 27]. A review on optical methods used for the observation of surface and volumetric waves is presented by Monchalin [41].

An example of the interferometric method, is the work of Aussel *et al.* [42] in which a theoretical description for elastic waves generation is carried out in ablative and thermoelastic regimes, for a quasi-point laser source. The experimental apparatus used is shown in Fig. 2.1 [42]. A Nd:YAG laser operating at 1064 nm with 10 ns and 20 ns pulse time duration was used. The excitation laser was focused at the sample. The acquisition system was synchronized by a trigger photodetector. The elastic waves were probed by a Michelson interferometer, where the detectable bandwidth was from 10 kHz to 50 MHz. The obtained results are in good agreement with the calculations. Other authors used similar interferometric method to probe elastic waves: Spicer and Hurley [9], Goruk [43], Draeger *et al.* [44], Royer *et al.* [45], Graebner [46], and Hashimoto [47].

Spicer and Hurley [9] used laser pulses to generate thermoelastic waves and probed the resulting deformation in the center and in regions near the illuminated area. The experiment was carried out on a 10 mm thick aluminum sample. A reproduction of the experimental diagram used in their work is presented in Fig. 2.2. A Nd:YAG pulsed laser

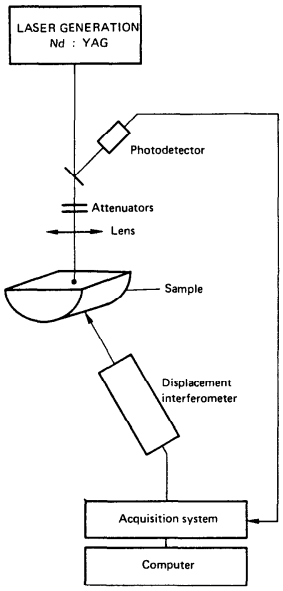

Figure 2.1: Experimental apparatus diagram used by Aussel *et al.* [42]. Reproduction of original, page 250.

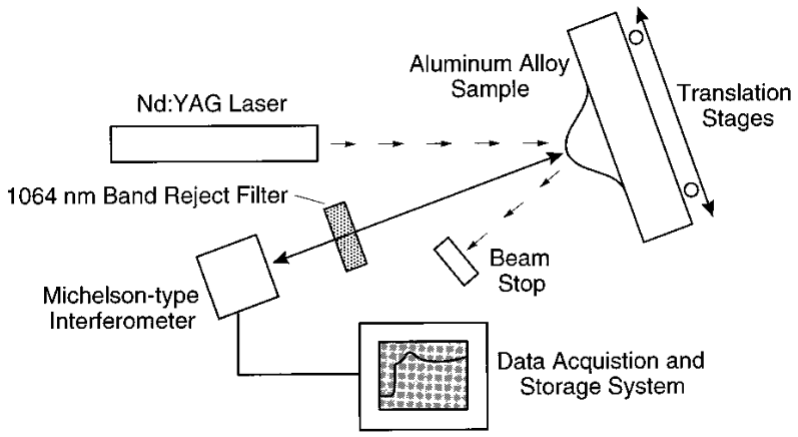

Figure 2.2: Experimental apparatus diagram used by Spicer and Hurley [9]. Reproduction of original, page 3651.

operating at 1064 nm was used as the source of thermoelastic waves. The incidence angle between the excitation laser to the normal axis of the surface was set up to be 20°. Surface displacements were measured using a Michelson interferometer. The experimental data and the numerical results were in good agreement.

The optical method described by Engan in 1978 [48] is an improvement of the method known as knife-edge described by Adler *et al.* [49]. In the knife-edge method, a laser beam with a diameter smaller than the acoustic wavelength is reflected from the probed surface. The surface waves cause a deflection in the beam that is probed by the knife-edge scheme. The signal that is provided by the detector has information about the phase and amplitude of the detected waves. However, in the experiment described

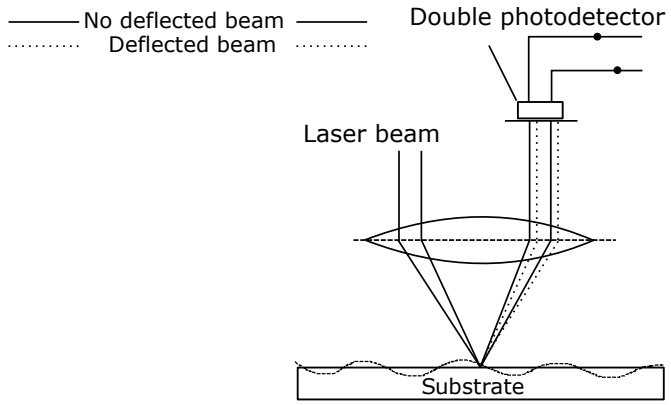

Figure 2.3: Experimental apparatus diagram used by H. Engan [48]. Reproduction of original, page 373.

by Engan [48], given in Fig. 2.3, the blade is replaced by a double photodiode and the signal obtained is the difference of the electric voltage between the two photodiodes when the beam is deflected. Engan [48] argues that this apparatus, when used with the double photodiode has several advantages, such as the decrease of the optical components to be aligned and improving the signal-to-noise ratio. Other researchers also make use of similar techniques in their works, such as Kavalerov *et al.* [50], Rooth *et al.* [51], Kamizuma *et al.* [52] and Hashimoto *et al.* [53].

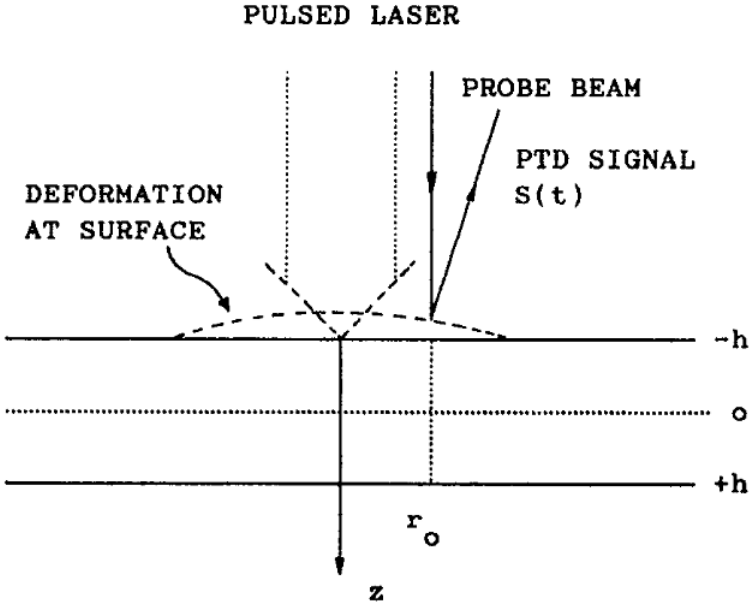

Figure 2.4: Experimental apparatus diagram used by Cheng *et al.* [27]. The sample have thickness 2h, o is the center of sample in relation to the azimutal axis z, and r_{o} is the distance between the center of illuminated area and the probe beam. Reproduction of original, page 717.

Cheng *et al.* [27] showed the behavior for thermoelastic waves detected by the photothermal deflection technique. The experimental diagram is presented in Fig. 2.4 and illustrates the excitation and detection schemes. A pulsed laser beam is used for the

generation of thermoelastic waves and another laser beam, with a smaller diameter, is also located on the surface in order to probe the deformations under the probing area by the photothermal deflection signal $S(t)$. The behavior of the deformation was studied as a function of the pulse width and the effect was compatible with the quasi-static approximation for the thermoelastic equation [40].

2.2 Thermoelastic Equation

The generic solution for the thermoelastic equation for a sample heated by a excitation laser beam is treated as described in Ref. [40]. The local variation of the temperature in a material, due to the absorption of the laser beam, generates a state of stress and strain that in turn cause an expansion or contraction of the material. The stress and strain states can be described by the symmetric tensors σ_{ij} and ϵ_{ij} respectively, where $i, j = 1, 2, 3$ represent the coordinates. Expansion or contraction, in turn, is described by the displacement vector $\vec{u}$ which has components u_i [40]. In framing the problem to the linear elasticity theory, the tensor of strain is related to the displacement vector [40, 54] by

$$\epsilon_{ij} = \frac{1}{2}\left(\frac{\partial u_i}{\partial x_j} + \frac{\partial u_j}{\partial x_i}\right), \; i, j = 1, 2, 3. \tag{2.3}$$

The stress tensor can be related with the strain tensor (and implicitly with the displacement u_i) by the relation

$$\sigma_{ij} = 2\mu_{\mathrm{l}}\epsilon_{ij} + (\lambda\epsilon_{kk} - \gamma_{\mathrm{m}}T_s)\delta_{ij}, \tag{2.4}$$

where $\gamma_{\mathrm{m}} = (3\lambda + 2\mu_{\mathrm{l}})\alpha_T$, α_T is the linear thermal expansion coefficient, λ and μ_{l} the Lame's coefficients, ${\epsilon_{kk}}^2$ the normal strain tensor summation, $T_{\mathrm{s}} \equiv T_{\mathrm{s}}(x_i, t)$ is the temperature change in the sample, and δ_{ij} is the Kronecker delta.

The total displacement due to the local temperature increase of sample can be determined from the set of Navier-Stokes displacement equations [40]

$$(\lambda + 2\mu_{\mathrm{l}})\nabla^2\vec{u} + (\lambda + \mu_{\mathrm{l}})\nabla \times (\nabla \times \vec{u}) = \gamma_{\mathrm{m}}\nabla T_{\mathrm{s}} + \rho_{\mathrm{s}}\frac{\partial^2\vec{u}}{\partial t^2}, \tag{2.5}$$

where $\rho_{\mathrm{s}}\dfrac{\partial^2\vec{u}}{\partial t^2}$ represents the inertia term [22]. The displacement vector $\vec{u}$ can be split, according to the Helmholtz decomposition, as [40, 54–56]

$$\vec{u} = \nabla\Phi + \nabla \times \vec{\psi}. \tag{2.6}$$

where Φ is the scalar displacement field and ψ is the displacement vector field.

[2] Throughout the work, the repeated indexes represent the summation notation, $A_{kk} = A_{11} + A_{22} + A_{33}$.

The displacement vector $\vec{u}$ representation as in Eq. (2.6), when substituted in (2.5), gives a set of two wave equations

$$\nabla^2\Phi - \frac{1}{c_{\mathrm{P}}^2}\frac{\partial^2\Phi}{\partial t^2} = mT_{\mathrm{s}} \tag{2.7}$$

and

$$\nabla^2\vec{\psi} - \frac{1}{c_{\mathrm{S}}^2}\frac{\partial^2\vec{\psi}}{\partial t^2} = 0, \tag{2.8}$$

where $m = (3\lambda + 2\mu_{\mathrm{l}})/(\lambda + 2\mu_{\mathrm{l}})$. The constants c_{P} and c_{S} are the propagation velocities of the waves related to the Eqs. (2.7) and (2.8) [40,54]. The representation of the wavefronts are shown in Fig. 1.1.

The velocity $c_{\mathrm{P}} = [(\lambda + 2\mu_{\mathrm{l}})/\rho_{\mathrm{s}}]^{1/2}$ represents the propagation velocity of an irrotational wave, which causes only volume changes. The particle displacement within the wave is the same of the wave propagation. These kind of waves are called longitudinal, primary or compression waves [2, 40, 54, 56]. The velocity $c_{\mathrm{S}} = (\mu_{\mathrm{l}}/\rho_{\mathrm{s}})^{1/2}$ describes the velocity of the secondary or transversal waves, related to a rotational movement such that the body elements experiences no change in the volume. The secondary waves cause displacements perpendicular to their propagation [2, 40, 54, 56].

Equation (2.7) can be described in terms of the potential displacement Φ. For this, the heat diffusion equation

$$\left(\nabla^2 - \frac{1}{D_{T\mathrm{s}}}\frac{\partial}{\partial t}\right) T_{\mathrm{s}}(x_i, t) = -\frac{Q}{D_{T\mathrm{s}}}, \tag{2.9}$$

is used together with the left side of Eq. (2.7), to obtain [40]

$$\left(\nabla^2 - \frac{1}{D_{T\mathrm{s}}}\frac{\partial}{\partial t}\right)\left(\nabla^2 - \frac{1}{c_{\mathrm{P}}^2}\frac{\partial^2}{\partial t^2}\right)\Phi = -\frac{mQ_{\mathrm{s}}}{D_{T\mathrm{s}}}. \tag{2.10}$$

Here, $D_{T\mathrm{s}}$ is the thermal diffusivity and Q_{s} is the heat source term of sample.

A useful method to solve the system of Eqs. (2.7), (2.10), and (2.8) is the use of Laplace integral transform[3] and Fourier integral transform[4] [40, 57]. However, depending on the source term $Q_{\mathrm{s}}(x_i, t)$ and the boundary conditions given by the geometry of the sample, an analytical solution is not always possible.

2.2.1 General Solution

A general solution can be obtained assuming that the displacement vector can be write as the sum $\vec{u} = \vec{u}^{\mathrm{p}} + \vec{u}^{\mathrm{h}}$, where $\vec{u}^{\mathrm{p}}$ is the particular solution and $\vec{u}^{\mathrm{h}}$ the homogeneous solution. The displacement potential is constituted by a part corresponding to the

[3] $\tilde{F}(x_i, s) = \int_0^\infty f(x_i, t)\exp(-st)\mathrm{d}t$

[4] $F^*(a_k, t) = (2\pi)^{-3/2}\int_{E_3} f(x_i, t)\exp(ia_k x_k)\mathrm{d}V$ with $\mathrm{d}V = \mathrm{d}x_1\mathrm{d}x_2\mathrm{d}x_3$

particular solution Φ_0 and another corresponding to the homogeneous solution ϑ. Thus, the Eq. (2.7) is solved for Φ_0, (2.8) for $\vec{\Psi}$, and the homogeneous wave equation for ϑ

$$\nabla^2\vartheta - \frac{1}{c_{\mathrm{P}}^2}\frac{\partial\vartheta}{\partial t} = 0. \tag{2.11}$$

By solving the set of equations and applying the correct boundary conditions for the problem, the expression for displacement vector $\vec{u}$ can be obtained.

Particular Solution

Initially, the Laplace and Fourier transforms are applied to the heat diffusion equation

$$-\left(a_k a_k + \frac{s}{D_{T\mathrm{s}}}\right)\tilde{T}_{\mathrm{s}}^* = -\frac{\tilde{Q}_{\mathrm{s}}^*}{D_{T\mathrm{s}}} \tag{2.12}$$

and to the Eq. (2.7),

$$-\left(a_k a_k + s^2\alpha_1^2\right)\tilde{\Phi}_0^* = m\tilde{T}_{\mathrm{s}}^*, \tag{2.13}$$

where $\alpha_1 = 1/c_{\mathrm{P}}$. The functions $\tilde{T}_{\mathrm{s}}^*$, $\tilde{\Phi}_0^*$, and $\tilde{Q}^*$ are the Laplace and Fourier transforms of the respective functions T_{s}, Φ_0, and Q_{s}. The initial conditions are $T_{\mathrm{s}}(x_i, 0) = 0$ and $\Phi_0(x_i, 0) = \partial\Phi_0(x_i, 0)/\partial t = 0$. The Eqs. (2.12) and (2.13) results in

$$\left(a_k a_k + s^2\alpha_1^2\right)\left(a_k a_k + \frac{s}{D_{T\mathrm{s}}}\right)\tilde{\Phi}_0^* = -\frac{m\tilde{Q}_{\mathrm{s}}^*}{D_{T\mathrm{s}}}, \tag{2.14}$$

so that we can obtain $\tilde{\Phi}_0$ by solving

$$\tilde{\Phi}_0(x_i, s) = -\frac{m}{D_{T\mathrm{s}}}(2\pi)^{-3/2}\int_{E_3}\frac{\tilde{Q}_{\mathrm{s}}^*(a_i, s)\exp\left(-ia_k x_k\right)\mathrm{d}W}{\left(a_k a_k + s/D_{T\mathrm{s}}\right)\left(a_k a_k + s^2\alpha_1^2\right)}, \tag{2.15}$$

with $\mathrm{d}W = \mathrm{d}a_1\mathrm{d}a_2\mathrm{d}a_3$. Equation (2.15) can be written as

$$\tilde{\Phi}_0(x_i, s) = -\frac{m(2\pi)^{-3/2}}{s^2\alpha^2 - s/D_{T\mathrm{s}}}\frac{1}{D_{T\mathrm{s}}}\left[\int_{E_3}\frac{\tilde{Q}_{\mathrm{s}}^*(a_i, s)\exp\left(-ia_k x_k\right)\mathrm{d}W}{\left(a_k a_k + s/D_{T\mathrm{s}}\right)} - \int_{E_3}\frac{\tilde{Q}_{\mathrm{s}}^*(a_i, s)\exp\left(-ia_k x_k\right)\mathrm{d}W}{\left(a_k a_k + s^2\alpha_1^2\right)}\right]. \tag{2.16}$$

The first integral in Eq. (2.16) is exactly the solution for the temperature variation in the Laplace space. The second integral can be understood as the solution of a differential equation in Laplace space for an auxiliary function S, namely

$$\left(\nabla^2 - s^2\alpha_1^2\right)\tilde{S} = -\frac{\tilde{Q}_{\mathrm{s}}}{D_{T\mathrm{s}}}, \tag{2.17}$$

where $S(x_i, 0) = \partial S(x_i, 0)/\partial t = 0$. Thus the solution to the potential displacement in the Laplace space is written as

$$\tilde{\Phi}_0(x_i, s) = -\frac{m}{s^2\alpha_1^2 - s/D_{T\mathrm{s}}}\left(\tilde{T} - \tilde{S}\right). \tag{2.18}$$

With the solution of the displacement potential Φ_0 the stress tensors σ_{ij}^{p} are determined, which are represented by the Eq. (2.4). Using the relations $u_i^{\mathrm{p}} = \partial\Phi_0/\partial x_i$ and $\epsilon_{ij}^{\mathrm{p}} = \partial^2\Phi_0/\partial x_i\partial x_j$ we obtain

$$\sigma_{ij}^{\mathrm{p}} = 2\mu_{\mathrm{l}}\left(\frac{\partial^2\Phi_0}{\partial x_i\partial x_j} - \delta_{ij}\frac{\partial^2\Phi_0}{\partial x_k^2}\right) + \rho_{\mathrm{s}}\delta_{ij}\frac{\partial^2\Phi_0}{\partial t^2}. \tag{2.19}$$

The complete solution of the problem is determined by solving the homogeneous wave equations and applying the boundary conditions to every specific case.

Homogeneous solution

To obtain the homogeneous solution of the displacement vector, it is assumed that

$$\vec{u}^{\mathrm{h}} = \nabla\vartheta + \nabla\times\vec{\psi}^{\dagger} \tag{2.20}$$

where $\vec{\psi}^{\dagger} = \nabla\times\vec{\psi}$. Equation (2.8) has to be solved for each component i as a scalar function, defining the propagation direction of the wave. However, since the secondary wave does not change the sample volume, we get $\nabla\cdot\vec{\psi} = 0$ and thus

$$-\nabla\times\nabla\times\vec{\psi} - \frac{1}{c_{\mathrm{S}}^2}\frac{\partial^2\vec{\psi}}{\partial t^2} = 0. \tag{2.21}$$

To obtain the displacement direction, that is perpendicular to the wave propagation, one can apply the curl to the vector $\vec{\psi}$ obtained. The stress components related to the displacement vector $\vec{u}^{\mathrm{h}}$ are

$$\sigma_{ij}^{h} = 2\mu_{\mathrm{l}}\epsilon_{ij}^{\mathrm{h}} + \lambda\frac{\partial^2\vartheta}{\partial k\partial k}. \tag{2.22}$$

where the strain tensor $\epsilon_{ij}^{\mathrm{h}}$ is defined by the Eq. (2.3) and the last term represents the sum of the second derivatives in each direction.

Mode conversion

When mechanical waves are obliquely incident at the interface between a solid and air (or a free surface) these waves undergo refraction and reflection. Conversion between wave types occurs with reflection, i.e., a P-wave incident with an angle θ_{P} relative to the vector normal to the incident surface generates a S-wave with an angle of reflection θ_{S} and vice-versa [58]. The relation between the angles of incidence and reflection of such

waves is described by Snell's law [29].

$$\frac{\sin\theta_{\mathrm{P}}}{c_{\mathrm{P}}} = \frac{\sin\theta_{\mathrm{S}}}{c_{\mathrm{S}}}. \tag{2.23}$$

There is a critical angle θ_{c} that determines the incidence limit to the existence of refraction from a medium to other. This angle is defined by

$$\sin\theta_{\mathrm{c}} = \left(\frac{c_{\mathrm{S}}}{c_{\mathrm{P}}}\right), \tag{2.24}$$

so that when $|\theta| = \theta_{\mathrm{c}}$ the refraction angle of the P wave, θ_{P} is $\pi/2$.

Head waves

In the region $|\theta| > \theta_{\mathrm{c}}$, due to the above mentioned boundary condition, a lateral wave, or Head wave (H-wave) or conic wave is observed, and its wavefront is parallel to the line PS [2] shown in Fig. 1.1. Additionally, according to the definition given by Aussel [42], the H-wave can be considered as a wave that arises from a P-wave that propagates at the fluid/solid interface and generates a S-wave along its entire path in the direction of the critical angle. The propagation velocity of a H-wave is given by [42]

$$c_{\mathrm{H}} = \frac{c_{\mathrm{P}}}{\left[c_{\mathrm{P}}\cos\theta\left(\frac{1}{c_{\mathrm{S}}^2} - \frac{1}{c_{\mathrm{P}}^2}\right)^{1/2} + \sin\theta\right]}. \tag{2.25}$$

This type of wave radiates its energy towards the interior of the sample and its amplitude decreases very quickly when moving away from its source [2].

Rayleigh waves

The waves that propagate near the material surface are the Rayleigh waves or R-waves [5, 31, 40, 54]. Nowacki [40] presented a mathematical deduction for R-waves and the relation of its velocity to the volumetric waves considering temperature coupling with strain fields. However, it is possible to obtain mathematically such waves even without considering the temperature-strain field coupling.

The velocity equation of the R-wave obtained without considering heat changes and temperature/strain field coupling, is described as

$$\frac{c_{\mathrm{R}}^3}{c_{\mathrm{S}}} + 4\frac{c_{\mathrm{S}}^3}{c_{\mathrm{R}}} = 4c_{\mathrm{R}}\left(c_{\mathrm{S}}^3\left(\frac{1}{c_{\mathrm{R}}^2} - \frac{1}{c_{\mathrm{P}}^2}\right)^{1/2}\left(\frac{1}{c_{\mathrm{R}}^2} - \frac{1}{c_{\mathrm{S}}^2}\right)^{1/2} + c_{\mathrm{S}}\right). \tag{2.26}$$

The c_{R} velocity is given by the positive real root of the above equation, that depends only of the c_{P} and c_{S} velocities, and is smaller than such velocities. A good approximation is

given by [42, 56]

$$c_{\mathrm{R}} = \frac{0.862 + 1.14\nu}{1 + \nu} c_{\mathrm{S}}. \tag{2.27}$$

2.3 Thermoelastic waves detection by photothermal mirror method

2.3.1 Theory

The Photothermal Mirror (PTM) method is a remote pump-probe technique used for the characterization of thermal, optical and mechanical properties of solids and liquids [21–23, 59–70]. Two nearly collinear laser beams are placed on the surface of the sample as shown in Fig. 2.5. An excitation beam is used to induce local heating of the material. The thermal gradient induces a thermal expansion (or contraction) that results in a surface deformation of the sample. Surface deformation acts as an optical element causing a phase shift to a probe laser beam, which is propagated over a long distance and detected by a photodetector-pinhole assembly. The sensor detects only the intensity variation in the center of the probe laser beam defined by the size of a circular apperture [21, 59].

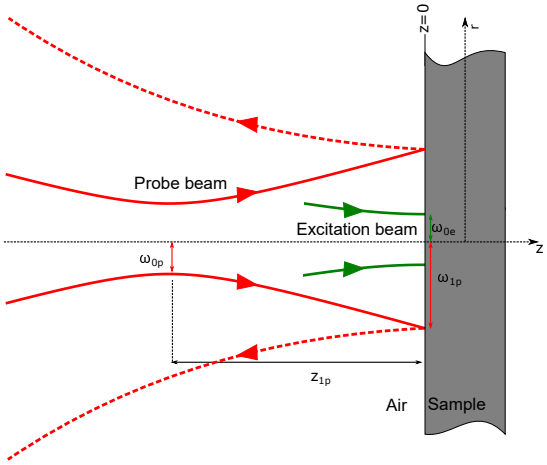

Figure 2.5: Schematics of the Photothermal Mirror (PTM) method showing the position of the sample in relation to the excitation and probe beams. $z_{1\mathrm{p}}$ is the distance between the focus of the probe beam (with radius $\omega_{0\mathrm{p}}$) and sample surface, ω_{e} is the radius of the excitation beam at the surface of the sample, $\omega_{1\mathrm{p}}$ the radius of the probe beam on the surface of the sample.

When the excitation beam excites the sample, which is submerged in a non-absorptive fluid (air, water, noble gas, etc.), part of the energy is reflected and part absorbed by the material. Light absorption is converted into thermal energy inducing a local increase in temperature. Due to thermal contact with the fluid, thermal energy is also transferred from the sample to the fluid surrounding by thermal conduction. The temperature vari-

ation in both media can be described by the solution of the heat diffusion equation [64]

$$\left(\nabla^2 - \frac{1}{D_{Ti}}\frac{\partial}{\partial t}\right) T_i(x_j, t) = -\frac{Q_i(x_j, t)}{D_{Ti}}, \tag{2.28}$$

where $i = \mathrm{s}$ for sample and $i = \mathrm{f}$ for the fluid. $D_{Ti} = k_i/(\rho_i C_{pi})$ is the thermal diffusivity, k_i is the thermal conductivity, ρ_i is the mass density, and C_{pi} is the specific heat. $T_i(x_j, t)$ is the temperature change in the material and $Q_i(x_j, t)$ is the heat source.

The source term of Eq. (2.28) depends on the radial and temporal profile of the excitation laser beam used, and on the optical absorption at the excitation wavelength. Here, a pulsed laser beam with a Gaussian radial profile, mode TEM_{00}, is used. Optical absorption of the material follows Beer's law, that is, the intensity of the laser beam decays exponentially along the depth of the sample. Here, the use of the cylindrical coordinates is convenient due to the axial symmetry of the beam. Assuming that the sample is positioned in the half space $z \geq 0$ and centered on $r = 0$, the source term for the sample can be approximated to have a radial and temporal Gaussian distribution of energy [22, 23],

$$Q_{\mathrm{s}}(r, z, t) = \frac{2Q_{0\mathrm{s}} \exp\left[-\left(\frac{2r^2}{\omega_{\mathrm{e}}^2} + \beta_{\mathrm{s}} z + \frac{(t-\xi_{\mathrm{p}})^2}{\tau_{\mathrm{p}}^2}\right)\right]}{\tau_{\mathrm{p}}\sqrt{\pi}\,[1 + \mathrm{erf}(\xi_{\mathrm{p}}/\tau_{\mathrm{p}})]}, \tag{2.29}$$

since it is a good approximation compared to the experimental radial and temporal profiles of the pulse [22, 23]. ω_{e} is the excitation beam radius on sample surface, β_{s} is the optical absorption coefficient of sample, τ_{p} is the pulse width, $\xi_{\mathrm{p}} = 3\tau_{\mathrm{p}}$ is the time of maximum irradiance of the pulse, and $\mathrm{erf}(x)$ the error function. $Q_{0\mathrm{s}} = 2E_{\mathrm{n}}(1 - R_{\mathrm{s}})\beta_{\mathrm{s}}\phi/(C_{p\mathrm{s}}\rho_{\mathrm{s}}\pi\omega_{\mathrm{e}}^2)$, E_{n} is the laser pulse energy, R_{s} is the sample surface reflection, ϕ is the fraction of optical energy converted into heat [23]. As the fluid is considered non-absorbing, $\beta_{\mathrm{f}} = 0$ and consequently $Q_{\mathrm{f}} = 0$.

The expression for the temperature variation in the sample and the fluid can be obtained with the use of the integral transforms, with approximations for the source term and also on the thermal coupling [22, 23, 59, 64]. The initial condition assumes that there is no temperature variation in the sample and in the fluid before the laser pulse, i.e., $T_i(r, z, 0) = 0$. For the boundary conditions, it is assumed that there is heat exchange with the fluid at the sample/fluid interface and the sample is radially infinite as compared to the radial extension of the temperature variation, i.e., $k_{\mathrm{s}}\partial T_{\mathrm{s}}(r, z = 0, t)/\partial z = k_{\mathrm{f}}\partial T_{\mathrm{f}}(r, z = 0, t)/\partial z$ and $T_i(r \to \infty, z, t) = 0$ respectively.

The temperature rise causes a stress and strain state in the sample inducing a deformation that is described by the solution of the Navier-Stokes thermoelastic equation [40]

$$(\lambda + 2\mu_{\mathrm{l}})\nabla^2\vec{u} + (\lambda + \mu_{\mathrm{l}})\nabla \times (\nabla \times \vec{u}) = \gamma_{\mathrm{m}}\nabla T_{\mathrm{s}} + \rho_{\mathrm{s}}\frac{\partial^2\vec{u}}{\partial t^2}. \tag{2.30}$$

As seen in Section 2.2, the solution of this equation is not trivial. Solutions are often obtained by approximating the heat source term or even by using quasi-static approximation [22, 39, 40, 59]. The mechanical coupling between the sample and the air can be neglected due to the large impedance mismatch[5] between the two media.

The deformation generated by the increase of temperature in the sample and the resulting generated waves are detected by the probe laser that is incident on the surface of the sample collinear to the excitation beam. The surface of the sample is located at a distance $z_{1\mathrm{p}}$ from the focus of the probe beam, which has radius $\omega_{0\mathrm{p}}$. The radius of the probe beam at the sample surface is $\omega_{1\mathrm{p}}$. The surface deformation causes a phase shift of the probe beam that can be described as

$$\Phi_{\mathrm{TM}}(r,t) = \frac{4\pi}{\lambda_{\mathrm{p}}}[u_z(r, z=0, t)], \tag{2.31}$$

where λ_{p} is the wavelength of the probe beam in the medium between the surface of the sample and the detector.

After being reflected from the sample surface, the probe beam is propagated to a sensor located at a distance $z_{2\mathrm{p}}$ from the sample surface. The sensor is coupled to a pinhole which ensures only monitoring of the center of the probe beam. The intensity variation of the probe beam detected at the sensor due to the phase change generated by the deformation can be mathematically described using the Fresnel integral for the propagation of the electric field with the far field approximation [28, 72].

$$S(t) = \left| \int_0^\infty \frac{2r}{\omega_{1\mathrm{p}}^2} \exp\left[-(1+iV)\frac{r^2}{\omega_{1\mathrm{p}}^2} - i\Phi_{\mathrm{TM}}(r,t) \right] \mathrm{d}r \right|^2, \tag{2.32}$$

where $V = z_{1\mathrm{p}}/z_{\mathrm{cp}} + z_{\mathrm{cp}}/z_{2\mathrm{p}}\,(1 + (z_{1\mathrm{p}}/z_{\mathrm{cp}})^2)$ and z_{cp} is the confocal distance of the probe beam.

The expression (2.32) connects directly the theory with the experimental data, giving information on the optical, mechanical and thermal properties of the sample. Eq. (2.32) can be evaluated numerically using the calculated surface deformation field $u_z(r, z=0, t)$. Additional phase shift to the probe beam as a consequence of the thermal lens effect created in the surrounding air by heat coupling to the sample, or the influence of the temperature dependence of the physical properties of the samples on the signal, can be safely neglected for the experiments performed in this study.

[5] The impedance of an acoustic medium is defined by $Z_i = \rho_i c_i$, where the index i represents de the medium, ρ_i the mass density, and c_i the longitudinal or transversal velocity of the wave [71]. For air, the impedance is $Z_{\mathrm{air}} = 409.783\,\mathrm{Nsm}^{-3}$ and $Z_{\mathrm{cooper}} = 4.135 \times 10^7\,\mathrm{Nsm}^{-3}$, for cooper.

The amplitude reflectance of the waves from the metal to the air is defined by $R = (Z_{\mathrm{metal}} - Z_{\mathrm{air}})/Z_{\mathrm{metal}} + Z_{\mathrm{air}})$ [71]. For the examples for air and cooper, the reflectance is $R = 0.99998$.

2.3.2 Results and discussion

The comparison between theory and experimental results is fundamental to verify where the theory is experimentally valid and how does the experiments can be useful to improve the theory. In throughout of this work all results are based on the experimental configuration described as follows. The pump-probe configuration of the photothermal mirror experiment is schematically described in Fig. 2.6. The pulsed laser (Q-switched Nd:YAG laser; Quantel, Brilliant B at 532 nm, $\xi_p = 45$ ns and $\tau_p = 15$ ns) is arranged almost collinear to the probe laser beam (He-Ne laser; Newport at 632.8 nm). The intensity variation of the probe beam center after reflection was detected by a pinhole-laser line filter-photodetector (Newport, Model 818BB-22) assembly in the far field. A digital oscilloscope (Tektronix, Model DPO 4102B) triggered by the photodiode (Newport, Model 818BB-22) recorded the data. Due to the wide frequency bandwidth (DC to 200 MHz) of this homodyne detection method, both the fast transients, such as the propagation elastic waves, and the slower thermal-diffusion-driven changes of the surface displacement can be monitored by a single stand-off detector.

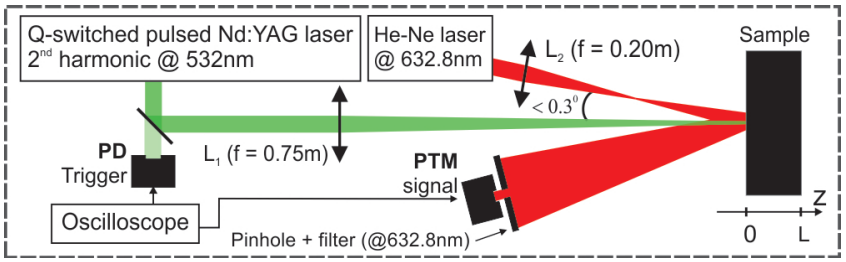

Figure 2.6: Experimental diagram for the PTM measurements. The pump and probe beam are focused by biconvex lenses of focal lengths f. Experimental parameters are $\omega_e = 130\,\mu$m, $\omega_{1p} = 580\,\mu$m, $z_{cp} = 3.3$ cm, and $z_{1p} = 25.6$ cm. The temperature of the samples was 298 K.

Experimental PTM signals were generated on copper (UNS C10100) and aluminum (UNS A6061) disks of 1.6 cm in diameter and thickness L. The surface of the samples were manually polished to a mirrored surface. The surface reflectance (R_s) of each sample at 532 nm was obtained using a spectrophotometer (Perkin Elmer, Model Lambda 1050) equipped with an integrating sphere (Labsphere, Model #150MM RSA ASSY) and the results are shown in Table 2.1

Since the samples used in this work are metals, the optical absorption coefficient is approximately in the order of 10^7 m^{-1} [23]. Thus, the incident light of the excitation beam is absorbed in most part close to the sample surface. The Beer's Law term, $\exp(-\beta_s z)$, in source term of heat diffusion equation, can be substituted by a Dirac Delta function, i.e., $2\delta(z)/\beta_s$ [23,59], which simplifies the calculations requiring less computational processing in the numerical evaluation of the PTM signal. All calculations performed during this work are performed using this condition. Numerical comparisons for the temperature variation under pulsed excitation considering different optical absorption coefficients were recently

Table 2.1: Physical properties used in all numerical calculations throughout the work. The velocities c_{P}, c_{S} e c_{R} are calculated from the theoretical values of ρ_{s}, Y, and ν [73].

Parameters	Cooper (UNS C10100)	Aluminum (UNS A6061)
k_{s} ($\mathrm{Wm^{-1}K^{-1}}$)	387	155
ρ_{s} ($\mathrm{kgm^{-3}}$)	8887	2700
C_{ps} ($\mathrm{Jkg^{-1}}$)	383	1020
α_T ($10^{-6}\mathrm{K^{-1}}$)	16.7	22.8
Y (GPa)	126	69
ν	0.338	0.331
R_{s}	0.61	0.92
Calculated velocities from ρ_{s}, Y, and ν		
c_{P} ($\mathrm{ms^{-1}}$)	4653	6165
c_{S} ($\mathrm{ms^{-1}}$)	2302	3098
c_R ($\mathrm{ms^{-1}}$)	2148	2888

studied [23], showing a good agreement for the approximation of surface absorption for optical absorption coefficients greater than $10^7\,\mathrm{m^{-1}}$.

Temperature change, displacement, velocity fields can be obtained from numerical calculations using finite element method (FEM). Intensity PTM signals also can be obtained with additional computation using Fresnel integral. For this, the heat diffusion and thermoelastic equations were solved using COMSOL MULTIPHYSICS 4.3b software. The model was constructed using an axially symmetric 2D geometry. The numerical calculations were performed considering the actual sample size, thermal coupling between the sample and the air, and appropriate boundary and initials conditions. The parameters of each sample used in each calculation are listed in Table 2.1.

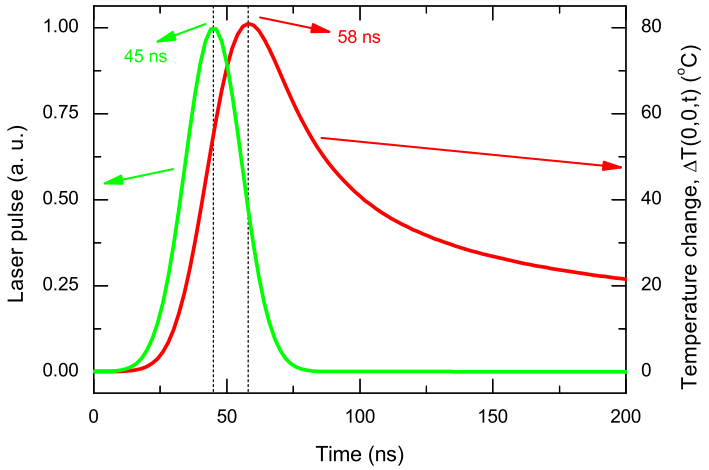

Figure 2.7: Time relationship between the temperature increase at $z = 0$ and $r = 0$, and the temporal shape of the excitation laser beam pulse. The pulse width is set to $\tau_{\mathrm{p}} = 15\,\mathrm{ns}$, the maximum irradiance time to $\xi_{\mathrm{p}} = 45\,\mathrm{ns}$ and energy to $E_{\mathrm{n}} = 40\,\mu\mathrm{J}$. The parameters used for the calculations are those of the copper sample, according to Table 2.1.

Figure 2.7 shows the time relationship between temperature increase at $r = 0$ and $z = 0$ and the temporal shape of the excitation laser beam pulse. It is observed that, if the free parameters of the excitation laser pulse are set to $\tau_p = 15\,\text{ns}$ and $\xi_p = 45\,\text{ns}$, the temperature reaches its maximum value in approximately $t = 58\,\text{ns}$, i. e., after approximately 89% of the total incident energy of pulse is delivered to the sample. The temperature variation was obtained by means of numerical calculations for copper with the physical properties as presented in Table 2.1 and a pulse with energy of $40\,\mu\text{J}$, which is close to the maximum energy used in the experimental measurements carried out. Despite the large temperature rise (approximately 80° C), physical properties of the samples vary about 6%, that is not enough to alter the physical state of the region radiated by the pulse, ensuring thermoelastic regime.

Experimental PTM signals were generated on samples irradiating focused laser pulses with energies varying from $10\,\mu\text{J}$ to $50\,\mu\text{J}$. The PTM signals presented in Fig. 2.8 are the average of over 100 transients at a repetition frequency of 10 Hz. The time interval between consecutive events is long enough[6] for the sample to return to its original state. The transients show the intensity change of the central portion of the continuous probe beam reflected from the sample surface at the far field sensor. The energies and experimental parameters are listed in the figures.

The PTM signal is a complex convolution of the probe beam wavefront distortion caused by the surface displacement. Its shape can be quantitatively assessed by comparing the experiments to the theoretical signal given by Eq. 2.32. The heat diffusion and the thermoelastic equations were numerically evaluated by the finite element analysis (FEA) method using the software Comsol Multiphysics 4.3b. The model was built in the 2D axisymmetric geometry and employed to solve Eq. 2.28 and Eq. 2.30 with a realistic sample geometry assuming heat coupling from metal to air with appropriated boundary and initial conditions, and the physical properties of the samples [73]. Numerical results for $u_z(r, 0, t)$ are then used to calculate the probe beam wavefront distortion and the PTM signal, Eq. 2.32. Continuous lines in Fig. 2.8 show the calculated PTM signals. The numerical predictions are in good agreement with measurements, presented by circles. By comparison, the calculated PTM signal without the inertia term in Eq. 2.30, known as the quasi-static approximation [22], is also presented with dashed lines.

The laser pulse generates various thermoelastic waves that can be seen in Fig. 2.9 by assessing the FEA calculated radial $v_r(r, z, t)$ and axial $v_z(r, z, t)$ components of the particle velocity field, with $v_j(r, z, t) = \partial u_j(r, z, t)/\partial t$. The velocity fields represent the wavefronts at successive times after the interaction. Soon after the pulse is absorbed, mechanical waves are indistinguishable in the bulk of the sample. In the far field, just

[6]The interval of 100 ms between each transient is about 200 times longer than the time where the sample reach the unperturbed state again. For comparison with Ref. [23], the time for the samples reach the original state after excited by the approximately same conditions of this thesis are about 0.5 ms.

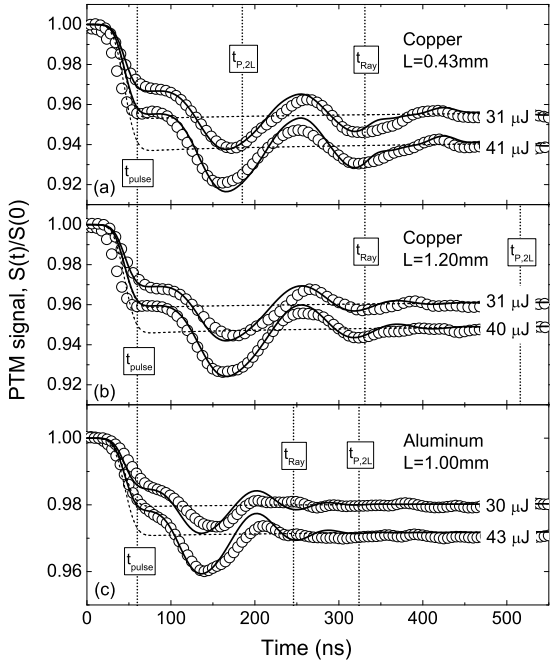

Figure 2.8: Measured (circles) and FEA calculated (lines) PTM signal for (a-b) copper and (c) aluminum metals with different thicknesses L. Dashed lines represent the FEA calculated signal without the inertia term in Eq. 2.30. Vertical lines denote: the end of illumination (t_{pulse}), the return time of flight of the P-wave across the thickness of the plate ($t_{\mathrm{P,2L}}$), and time at which the Rayleigh wave leaves the probed area (t_{Ray}). Physical properties are listed in Table 2.1

.

before the P-wave reaches the opposite side of the illuminated surface, at 240 ns, for the case presented in Fig. 2.9, separate wave-types clearly decouple and different types of the elastic waves can be identified. Their propagation velocities (c_{P},c_{S},c_{R}) are listed in Table 2.1. Before the time the P-wave reflects back to the illuminated surface at $t_{P,2L} = 2L/c_{\mathrm{P}}$ (Fig. 2.8), only the surface propagating P-, S-, and R-waves distort the probing beam. After this time, the multiply reflected (2P, 2S, 4P, ...) and mode converted bulk waves (PS, 3PS, ...) arrive to the front surface additionally affecting the shape of the thermal mirror. t_{Ray} in Fig. 2.8 labels the time $t_{\mathrm{Ray}} = (\omega_{\mathrm{e}} + \omega_{1\mathrm{p}})/c_{\mathrm{R}}$ when the slowest propagating surface waves, the R-waves originating from the far edge of the interaction zone, leave the central part of the probing area. t_{pulse} marks the end of illumination ($t_{\mathrm{pulse}} \approx 75$ ns).

One can see from Fig. 2.8 that as long as the surface waves propagate within the probed area, the modeled PTM signals conform to the measured ones if the inertial term is included and largely deviate when this term is excluded. When the surface waves exit the probing spot, the inclusion of the inertial term gives almost identical results as if it was not taken into account. Furthermore, the bulk waves reflected from the opposite surface does not affect the probing surface because their wavefronts are nearly parallel with the surface and cause a large curvature displacement of the whole probing area. The PTM method is almost insensitive to the uniform nanometer range out of plane motion of the whole sample.

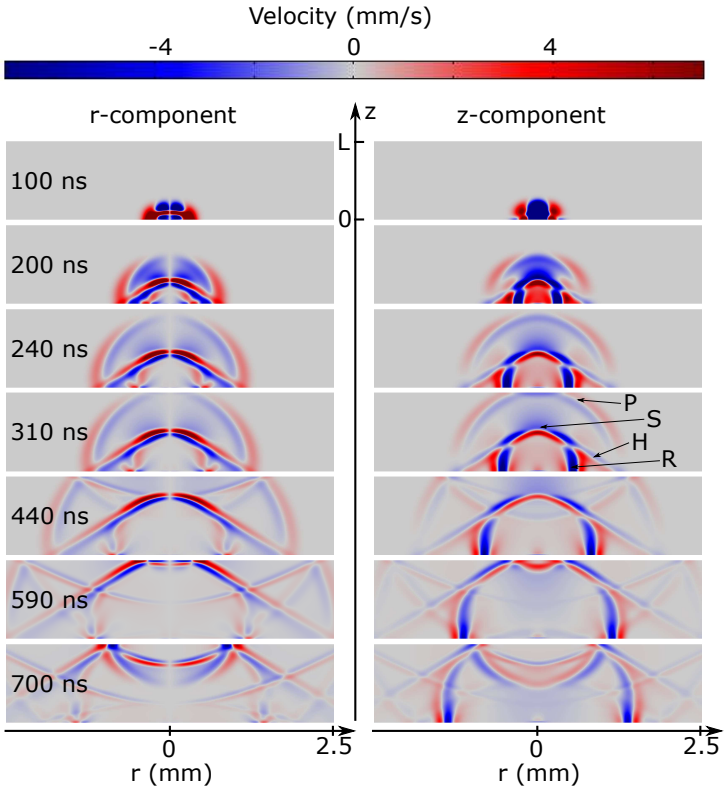

Figure 2.9: Simulated velocity field time frames, $v_r(r, z, t)$ and $v_z(r, z, t)$, for copper with $L = 1.20\,\text{mm}$.

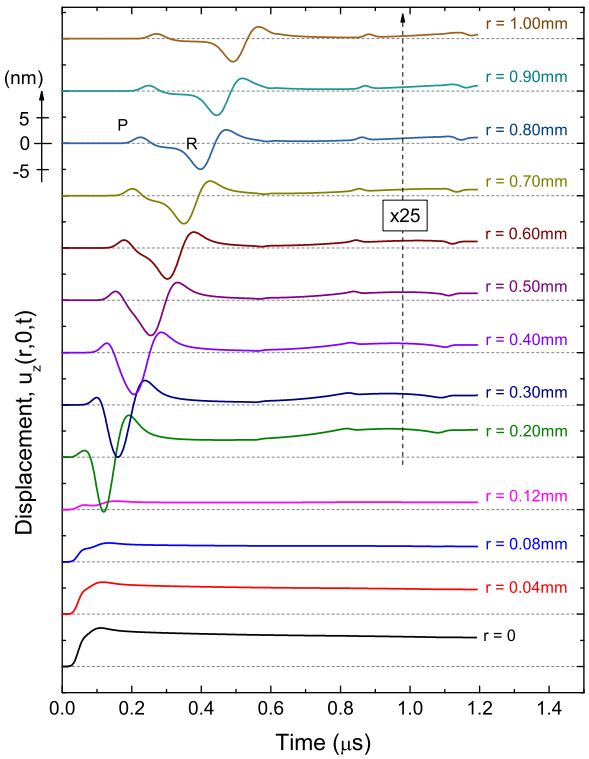

Figure 2.10: Simulated surface displacement for copper with $L = 1.20\,\text{mm}$ at different distances r from the epicenter. Positive $u_z(r, 0, t)$ means outward displacement.

Figure 2.10 shows the time dependence of the modeled (FEA calculated) surface displacement, $u_z(r, 0, t)$, at different distances r from the epicenter. At the epicenter, $r = 0$ and $z = 0$, heat is locally deposited by the pulse on the surface and thermal expansion governs the displacement of the surface [9]. Large displacements of 7 nm are created around the vicinity of the excitation area. Elastic waves are resolved away from the epicenter as shown for $r > 0.60$ mm. For example, at $r = 1.00$ mm the surface skimming P-wave arrives at about 250 ns. The R-wave follows between 400 ns and 600 ns, and then the reflected bulk waves arrive. The outward P-wave displacement followed by the inward phase of the R-wave is a clear signature of elastic waves generated by thermal expansion [2, 3]. If the initial phase of the R-wave was outward, the dominating source would be either ablation or radiation pressure, while the latter never dominates in metals.

The probe beam reflected from the sample senses the complex surface out of plane deformation history displayed in Fig. 2.11. The illuminated area experiences a large, long-lasting swelling that is responsible for the overall decrease of the PTM signal. Superimposed on this dominating effect, different radial annuli of the probed beam can be either focused (positive displacement slopes of the surface propagating waves) or dispersed (negative slopes). This in turn leads to the increase or decrease of the intensity that passes through the pinhole placed in front of the detector.

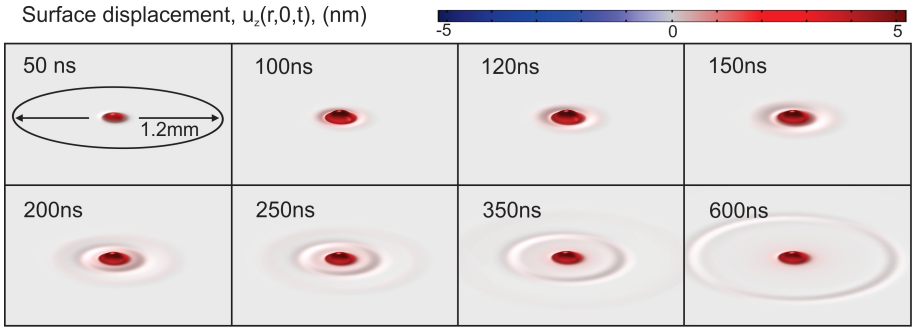

Figure 2.11: Simulated time evolution of the surface displacement of copper ($L = 1.20$ mm).

The spatial and temporal dependence of the propagation of the waves, and consequently the deformation caused in the sample can be investigated as a function of the thickness L. The surface deformation $u_z(0, 0, t)$ for four different thicknesses, $L = 0.30$ mm, $L = 0.43$ mm, $L = 0.90$ mm, and $L = 1.20$ mm are shown in Fig 2.12. The times $t_{\mathrm{P},nL}$ indicate the time that the P-wave needs to travel over the units of length nL of the sample. The same notation is used for the S-waves. We can observe that for times shorter than 700 ns, the samples of thicknesses 0.90 mm and 1.20 mm do not present differences in the behavior of the surface displacement in $r = 0$.

When the thickness of the sample decreases, the surface deformation $u_z(0, 0, t)$ behaves differently from that seen previously. The initial surface expansion is similar to the thicker samples for times shorter than 200 ns. However, since a simultaneous arrival of the fourth reflection of the P-wave, $t_{\mathrm{P},4L}$, with the second reflection of the S-wave, $t_{\mathrm{S},2L}$ occurs,

new bulging deformations can be observed. The times at which this deformation occurs for a sample of $L = 0.43\,\text{mm}$ is about 370 ns and for the sample of $L = 0.30\,\text{mm}$ is 258 ns. For times longer than 300 ns, we also observe that, for thinner samples with $L = 0.43\,\text{mm}$ and $L = 0.30\,\text{mm}$ in thickness, the amplitude of deformation $u_z(0, 0, t)$ after the excitation is larger than for the samples with thicknesses $L = 0.90\,\text{mm}$ and $L = 1.20\,\text{mm}$. This larger deformation amplitude may be due to the fact that, for smaller thicknesses, the samples tend to undergo deformation due to thermal expansion and additionally a large bending. This bending can be evaluated by constructing graphs of the deformation $u_z(0, L, t)$ on the second surface (the surface opposite to the illuminated one) of the sample (Fig. 2.13).

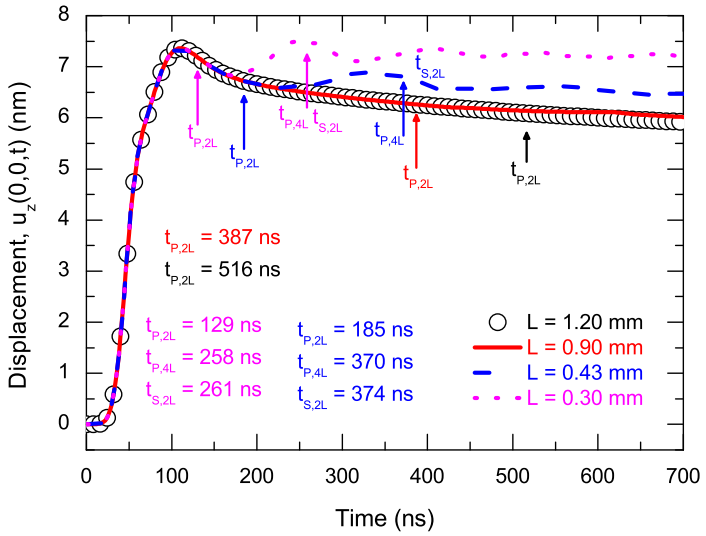

Figure 2.12: Surface deformation $u_z(0, 0, t)$ for different thicknesses L in cooper samples, with parameters listed in Table 2.1.

Figure 2.13 shows the induced deformation on the back surface of sample ($z = L$) at $r = 0$ as function of time, $u_z(0, L, t)$, for four sample thicknesses: $L = 1.20\,\text{mm}$, $L = 0.90\,\text{mm}$, $L = 0.43\,\text{mm}$, and $L = 0.30\,\text{mm}$. For the largest ones, $L = 0.90\,\text{mm}$ and $L = 1.20\,\text{mm}$, we observe that the induced bending is smaller than 0.5 nm, indicating that it does not effectively influence the sample surface deformation at $z = 0$. For times smaller than 700 ns we observe only the P and S-waves arrivals for $L = 1.20\,\text{mm}$, with times $t_{\text{P},L}$ and $t_{\text{S},L}$, respectively. Also, for $L = 0.90\,\text{mm}$, we can observe the first arrival of the P and S-waves with arrival times $t_{\text{P},L}$, $t_{\text{S},L}$ and the second arrival of the P-wave with time arrival $t_{\text{P},3L}$. We can also observe that the second arrival of P-wave on the opposite surface does not causes significant deformation for the sample with thickness $L = 0.90\,\text{mm}$. For $L = 0.43\,\text{mm}$ and $L = 0.30\,\text{mm}$, P-waves first arrivals are observed in times shorter than 100 ns. The second arrival of S-wave in L surface is also observed for times shorter than 700 ns, with time $t_{\text{S},3L}$. The deformation increases over time, which explains the bend caused in the sample, and that significantly influences the time evolution of the deformation of the illuminated surface of the sample.

Numerical calculations of wavefront velocity fields for thickness $L = 0.43\,\text{mm}$ are

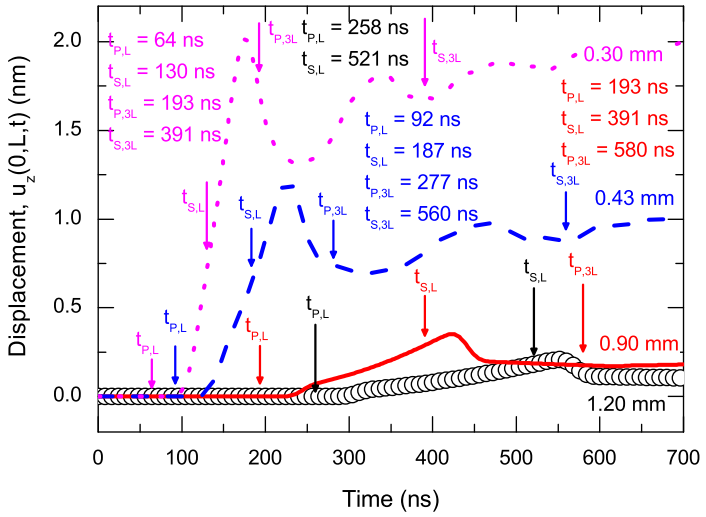

Figure 2.13: Back surface deformation $u_z(0, L, t)$ for different thicknesses L in cooper samples, with the parameters listed in Table 2.1. Positive values represent back surface $z = L$ contraction.

shown in Fig. 2.14. It is noted that the length of the wave $c_P t_{\text{pulse}}$ is comparable to the thickness of the sample, and the bulk waves arrive at the back surface of sample before being decoupled, causing reflections and interference that affects the deformations generated on both surfaces.[7] Such deformation can be observed along the radial length (r-axis) as a function of time on the sample surface ($z = 0$) (Fig. 2.15). These waves also have influence on the R-waves propagation along the sample surface for points $r > 0.30\,\text{mm}$. Another important detail is the amplitude increasing of the deformation over time. This increase in the amplitude is due to the bending caused by the temperature increasing in the sample, and is bigger when the thickness of the sample decreases, as seen in Fig. 2.13.

The wavefronts behavior within and on the surface of the sample is even more complex with the decrease of the sample thickness. Figure 2.16 shows the wavefronts velocity fields for $L = 0.30\,\text{mm}$. We can observe that the wavefronts are not distinguishable and that they interfere as they propagate within the sample, causing, in a general form, a very complex propagation for all subsequent reflections. These interferences, added to the bending caused by the small sample thickness, result in the pattern of deformations shown in Fig. 2.17 at $z = 0$ along r. The increase in the amplitude of the deformation is more pronounced when compared to the sample with $L = 0.43\,\text{mm}$, and the oscillations over time become more amplified.

All complexity shown in the previous figures for the velocity fields and consequently for the surface deformations along the entire sample, affect how the wavefront phase of the probe beam changes. To analyze the caused effects, numerical calculations using equation (2.32) were performed for the surface deformation $u_z(r, 0, t)$ for different thicknesses and the results are presented in Fig. 2.18.

[7] In such cases, the displacement field can be better described in terms of Lamb's waves [74].

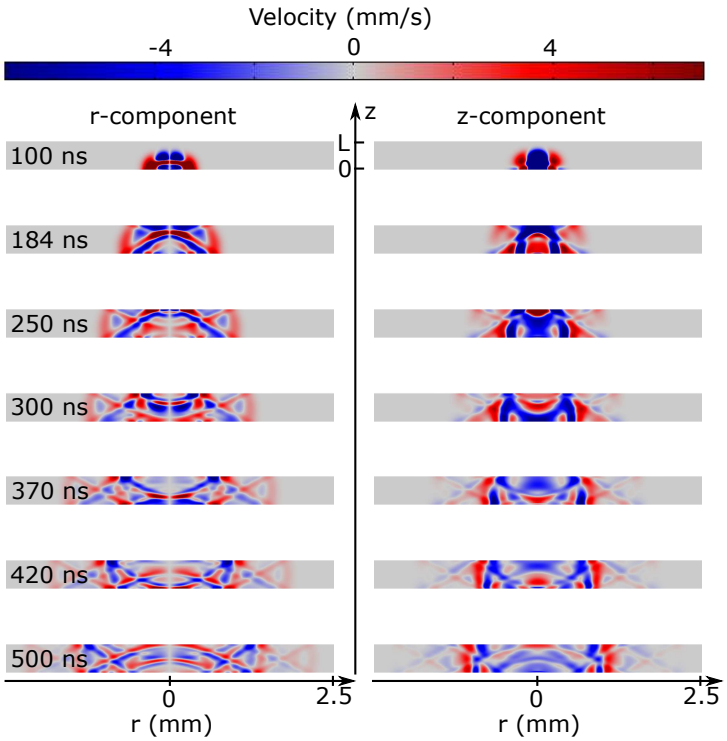

Figure 2.14: Simulated velocity field time frames, $v_r(r, z, t)$ and $v_z(r, z, t)$, for copper with $L = 0.43\,\text{mm}$.

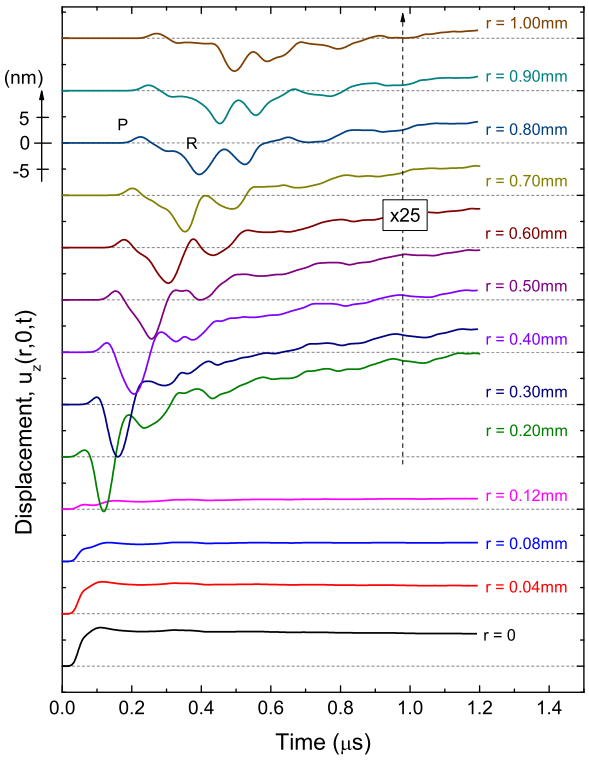

Figure 2.15: Simulated surface displacement for copper with $L = 0.43\,\text{mm}$ at different distances r from the epicenter. Positive $u_z(r, 0, t)$ means outward displacement.

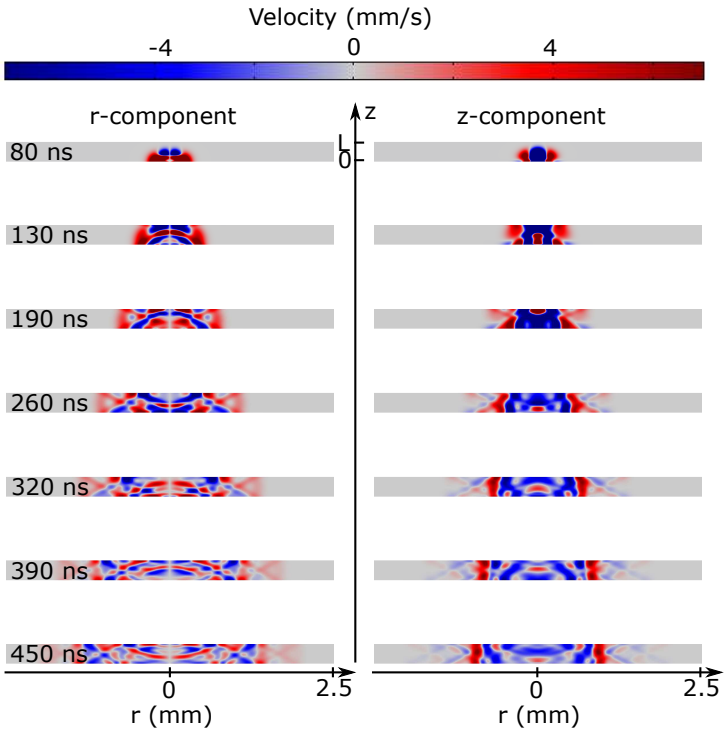

Figure 2.16: Simulated velocity field time frames, $v_r(r, z, t)$ and $v_z(r, z, t)$, for copper with $L = 0.30\,\text{mm}$.

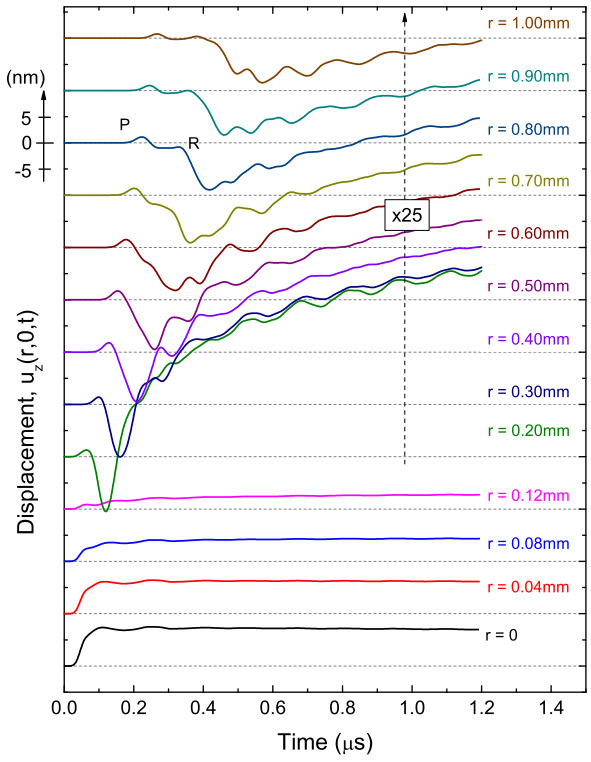

Figure 2.17: Simulated surface displacement for copper with $L = 0.30\,\text{mm}$ at different distances r from the epicenter. Positive $u_z(r, 0, t)$ means outward displacement.

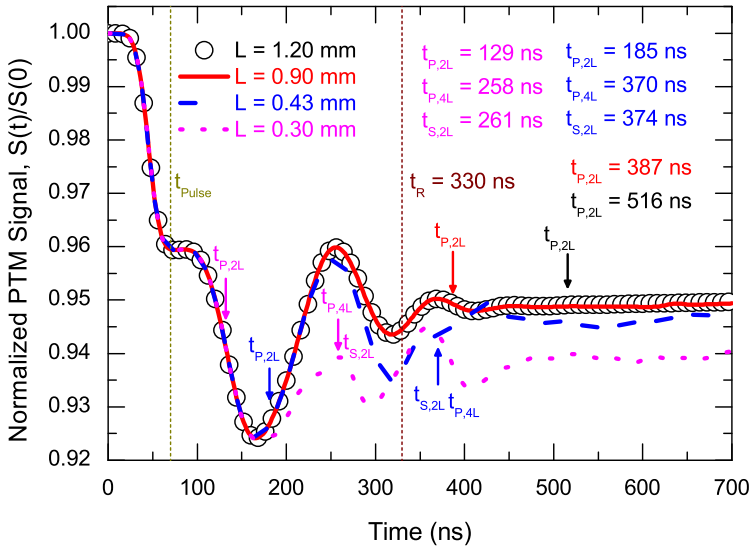

Figure 2.18: Normalized numeric PTM signal, as function of time for cooper samples, with different thicknesses L.

As already observed for the deformations at $z = 0$ and $z = L$, the intensity behavior of the probe beam in the photodetector for the sample $L = 0.90\,\text{mm}$ should be similar to that of the sample with $L = 1.20\,\text{mm}$. For $L = 0.43\,\text{mm}$, the transient behavior is slightly different compared to the thicker samples and can be observed in the experimental results presented in Fig. 2.8. The slight change in amplitude and shape for times longer than 300 ns is caused by the larger deformation over time due to the bending caused in the sample and the interferences of the wavefronts that affect the surface deformation. For $L = 0.30\,\text{mm}$ an even larger amplitude is noted for $200 < t < 300\,\text{ns}$. The valleys and peaks in this transient form a set of periodic oscillations, a fact that is probably linked to the interferences generated very quickly by the reflections on both surfaces of the sample.

2.4 Conclusion

We have shown that the applicability of the photothermal mirror method can be extended to visualize laser induced thermoelastic waves generated locally and propagating within metals. Heat deposition by the pulse launches bulk and surface waves and generates large surface swelling of the sample under the excitation area. Numerical solutions of the coupled heat diffusion and thermoelastic equations predict the detected photothermal mirror signal for copper and aluminum samples. Velocity field calculations show the moving wavefronts of various types of elastic waves inside the samples. Wavefront distribution is complex short after the pulse and decouples further in time evidencing internal reflection at the facets of the samples. The surface propagating waves, especially the Rayleigh wave, significantly affect the photothermal mirror signal, while the multiply reflected bulk waves only gently perturb the probed surface. The detection of elastic waves on top of

the large bulge enables characterization of thermal and also elastic properties of opaque solids. The thickness dependence on wave propagation within the samples shows that for thinner samples, i. e., the length of the P waves is comparable to the thickness of the sample, sample bending and multiple interference among the waves occur, modifying the PTM signal when compared to the thicker ones.

Chapter 3

Quantitative assessment of radiation force effect at the dielectric air-liquid interface[1]

In this chapter, we induce nanometer-scale surface deformation by exploiting momentum conservation of the interaction between laser light and dielectric liquids. The effect of radiation force at the air-liquid interface is quantitatively assessed for fluids with different density, viscosity and surface tension. The imparted pressure on the liquids by continuous or pulsed laser light excitation is fully described by the Helmholtz electromagnetic force density.

3.1 Introduction

The correct form of the momentum of light within dielectric materials and the effects caused by the radiation forces when light passes through adjacent media have been extensively debated for over a century [11–19]. Although the radiation pressure effects were predicted in 1871 [75], and experimentally observed in 1900 [76], a dilemma was created by controversial interpretations of the theories proposed by Minkowski in 1908 [77] and Abraham in 1909 [78] to explain the energy-momentum tensor of light. The history of the Abraham-Minkowski dilemma is intimately linked to the difficulties in sensing and interpreting the effects produced by radiation forces, which led to erroneous

[1]This chapter is totally reproduced from Capeloto, O. A. et al. "Quantitative assessment of radiation force effect at the dielectric air-liquid interface". Scientific Reports **6**, 20515 (2016); doi: 10.1038/srep20515, with the permission of Nature Publishing Group. The authorization letter is indexed in Appendix A.2

interpretations favoring one of the theories. This is based on the fact that both momentum descriptions have simple forms when light is incident from free space on a transparent and non-dispersive dielectric medium; Minkowski predicts a momentum in the medium proportional to its refractive index (n) and the photon momentum in the vacuum (p_0) as $p_{\mathrm{M}} = np_0$, while Abraham predictions is in the form $p_{\mathrm{A}} = p_0/n$. $p_0 = U/c$, U is the energy of light and c is the speed of light. The Minkowski-Abraham controversy has theoretically been resolved by the correct division of momentum between field and medium [11].

Early experimental investigations pursued answers to the dilemma, and continued to shed light on to this controversy. A number of reviews discuss these early experiments in details [11–19], although the conclusions derived favor either theory. For instance, Jones and coauthors [79] showed that a mirror submerged in a medium experiences a force consistent with each photon having the Minkowski momentum. Ashkin and Dziedzic [80] demonstrated that focused laser pulses created deformations of the water-air interface; the surface of the liquid experienced a net force outward from the water as predicted by Minkowski. Although, it was later assessed that the bulging of the liquid was also influenced by radial electrostriction forces [18, 81]. Walker and coauthors [82] measured the torque exerted on a disk suspended on a torsion pendulum. The experiments provide evidence in favor of the Abraham form. Zhang and coauthors [83] performed experiments based on Ashkin and Dziedzic [80] scheme. They show the interplay between Minkowski and Abraham forces illuminating water or mineral oil. On initial inspection, experimental results may appear to be in favor of one of the formulations. However, detailed analysis demonstrates explicitly and directly the equivalence of a number of different energy momentum tensors, provided the accompanying material tensor is taken into account [11,16]. Yet there has been so far only limited qualitative experimental tests of our understanding of radiative transfer between electromagnetic radiation and dielectric media. Quantitative measurements of the effects of radiation forces on dielectric media have attracted large interest with the advent of optical manipulation of micro-particles in fluid media and its potential application in biological systems.

Recently, Astrath and coauthors [28] measured surface deformation at the interface air-water generated by continuous and pulsed laser excitations using the photomechanical mirror (PM) method. The displacement caused by radiation forces was quantitatively described by the theory using the Helmholtz force density. The former experiment is a significant contribution to understanding of dynamics and momentum transfer in dielectric systems. The imparted pressure was found to have the same form as that using Minkowski momentum conservation at the interface between the dielectrics; a counterpart that could be though as propagating with the electromagnetic wave, the Abraham momentum, and that which is deposited locally in the material. The former statement would agree with running theories solving the controversial points of view regarding Abraham-Minkowski momentum formulations; this identifies the Abraham momentum as the kinetic momen-

tum and the Minkowski momentum as the canonical momentum [11]. Here, we measure precisely nanometer scale surface deformation using the photomechanical mirror method for a systematic study to assess quantitatively the effect of radiation force at the air-liquid interface of fluids with different physical properties. Additional measurements are performed to test Zhang's observations on the interplay between Abraham and Minkowski momenta.

3.2 Forces at a dielectric interface

The ponderomotive forces acting on a dielectric subjected to a non-uniform electric field can be written in terms of the stress tensor σ_{ik} and the momentum density G_i in the form [84]

$$f_i = \sum_k \frac{\partial \sigma_{ik}}{\partial x_k} - \frac{\partial G_i}{\partial t}. \tag{3.1}$$

For a dielectric fluid in the absence of free charge and current, the momentum density is $\vec{G} = \vec{E} \times \vec{H}/c^2$ and σ_{ik} is given by

$$\sigma_{ik} = -\frac{1}{2}\varepsilon_0 E^2 \left[\varepsilon_\mathrm{r} - \rho \left(\frac{\partial \varepsilon_\mathrm{r}}{\partial \rho}\right)_T\right] \delta_{ik} + \varepsilon_0 \varepsilon_\mathrm{r} E_i E_k. \tag{3.2}$$

The first term in Eq. 3.2 accounts for electrostriction. Eq. 3.2 leads to a force density [18, 78, 84]

$$\begin{aligned} \vec{f} &= -\frac{1}{2}\varepsilon_0 \langle E \rangle^2 \nabla \varepsilon_\mathrm{r} + \frac{1}{2}\varepsilon_0 \nabla \left[\rho \left(\frac{\partial \varepsilon_\mathrm{r}}{\partial \rho}\right)_T \langle E \rangle^2\right] \\ &+ \frac{\varepsilon_\mathrm{r} - 1}{c^2} \frac{\partial}{\partial t}\left(\vec{E} \times \vec{H}\right). \end{aligned} \tag{3.3}$$

$\vec{E}$ and $\vec{H}$ describe the electric and magnetic fields, ε_0 is the permittivity in vacuum, ρ is the mass density and $\varepsilon_\mathrm{r} = \varepsilon/\varepsilon_0$ is the relative permittivity of the medium.

The first term in Eq. 3.3 appears in both Minkowski and Abraham energy-momentum tensor formulations. This force acts where relative permittivity presents spatial variation. The second term accounts for the deformation (electrostriction) caused by the field inhomogeneity. The last term is known as the Abraham force density. This term is supposed to average to zero at optical frequencies and can be neglected in our model. In our experiments, the Abraham and Minkowski expression for the force are identical. This fact makes the Minkowski tensor, with the inclusion of the electrostriction term, an attractive formulation for experiments in optics [16, 85]. Thus, Eq. 3.3 reduces to the Helmholtz force [84, 86].

Here, we are considering a laser beam normally incident from air onto a flat surface

of a dielectric liquid. The pressure P imparted by the surface force can be calculated by integrating the normal component of $\vec{f}$ across the interface air/liquid as

$$P_{\text{in}} = \int_{-\delta}^{+\delta} \frac{1}{2}\varepsilon_0 \left\langle E_{\parallel} \right\rangle^2 \frac{\partial}{\partial z}\left[\rho\left(\frac{\partial \varepsilon_{\text{r}}}{\partial \rho}\right)_T - \varepsilon_{\text{r}}\right] \mathrm{d}z. \tag{3.4}$$

$\left\langle E_{\parallel} \right\rangle^2 = T_{\text{el}} \left\langle E_{\text{inc}} \right\rangle^2$ is the electric field tangential to the surface of the liquid, $T_{\text{el}} = 4n/(n+1)^2$ is the transmission coefficient, and E_{inc} is the incident electric field. In the limit of $\delta \to 0$, Eq. 3.4 results in a pressure P_{in} pushing the surface inwards as

$$P_{\text{in}} = \frac{1}{2}\varepsilon_0 \left\langle E_{\parallel} \right\rangle^2 \rho\left(\frac{\partial \varepsilon_{\text{r}}}{\partial \rho}\right)_T - \frac{1}{2}\varepsilon_0 \left\langle E_{\parallel} \right\rangle^2 (\varepsilon_{\text{r}} - 1). \tag{3.5}$$

The first term in Eq. 3.5 is the surface contribution of the electrostriction force, and the second term is numerically as the radiation pressure defined in the Minkowski momentum transfer formulation.

The radial volume electrostriction force is

$$f_{r,\text{V}} = \frac{1}{2}\varepsilon_0 \frac{\partial}{\partial r}\left[\rho\left(\frac{\partial \varepsilon_{\text{r}}}{\partial \rho}\right)_T \left\langle E_{\parallel} \right\rangle^2\right], \tag{3.6}$$

which counterbalances the inward displacement of the surface by the hydrostatic pressure P_{out} [18, 28, 87]

$$P_{\text{out}} = \frac{1}{2}\varepsilon_0 \rho\left(\frac{\partial \varepsilon_{\text{r}}}{\partial \rho}\right)_T \left\langle E_{\parallel} \right\rangle^2. \tag{3.7}$$

It leads to an overall pressure that elevates the surface of the liquid as [87]

$$P(r,t) = P_{\text{in}} - P_{\text{out}} = -\frac{2}{c}\left(\frac{n-1}{n+1}\right) I(r,t). \tag{3.8}$$

The field intensity is $I(r,t) = \varepsilon_0 cn \left\langle E_{\text{inc}} \right\rangle^2$. In fact, the volume contribution of the electrostriction is canceled out by its surface contribution [85], and surface deformation is described by that due to the Minkowski-Abraham term as well as those due to gravity and surface tension [19, 85]. $P(r,t)$ is an outward pressure effectively expanding the fluid, which is equivalent to assuming that the averaged momentum per photon is given by the Minkowski momentum [18] as the total propagating momentum. However, the Minkowski momentum can be thought as a sum of the Abraham momentum and the mechanical momentum of the medium [16, 85].

3.2.1 Surface deformation due to radiation forces

The pressure imparted on the liquid causes the displacement of its surface. Assuming that thermal effects caused by the laser absorption in the liquid is negligible for the over-

all surface deformation, the deformation can be calculated by solving the Navier-Stokes equation with appropriated boundary conditions. We used the finite element analysis (FEA) method for the numerical calculations using the software Comsol Multiphysics 4.3b with the "Laminar Two-Phase Flow, Moving Mesh" module for incompressible flow. This model solves the following equation

$$\rho\frac{\partial\vec{v}}{\partial t}+\rho\left(\vec{v}\cdot\nabla\right)\vec{v}=-\nabla P+\mu\nabla^2\vec{v}+\vec{F}. \tag{3.9}$$

$\vec{v}$ describes the flow velocity, P is the pressure, μ is the dynamic viscosity, and $\vec{F}$ is the volume force. The pressure $P(r,t)$ acts on the surface at $z=0$ parallel to the excitation beam. A complete FEA description is presented in Ref. [28]. The intensity distributions of the Gaussian excitation beams, continuous-wave and pulsed, modeled here are

$$I_{\mathrm{cw}}(r)=\frac{2P_{\mathrm{e}}}{\pi\omega_{\mathrm{e}}^2}e^{-2r^2/\omega_{\mathrm{e}}^2} \tag{3.10}$$

for the cw excitation, and

$$I_{\mathrm{pulsed}}(r,t)=\frac{2E_{\mathrm{n}}}{t_0\pi\omega_{\mathrm{e}}^2}e^{-2r^2/\omega_{\mathrm{e}}^2}e^{-(t-\xi_{\mathrm{p}})^2/\tau_{\mathrm{p}}^2} \tag{3.11}$$

for the pulsed excitation [24]. τ_{p} is the pulse width, ξ_{p} is the time to the maximum irradiance for the Gaussian pulse, $t_0=\tau_{\mathrm{p}}\sqrt{\pi}[1+\mathrm{erf}(\xi_{\mathrm{p}}/\tau_{\mathrm{p}})]/2$ is a normalization parameter, E_{n} and P_{e} are the pulse laser energy and continuous laser power, respectively, and ω_{e} is the radius of the excitation beam in the sample. The model was built in the 2D axisymmetric geometry. The external pressure and surface tension acts on the boundary condition of the free surface. The gravity vector enters the force term as $\vec{F}=\rho\,g\,\hat{z}$ with $g=9.79\,\mathrm{ms}^{-2}$ (as measured locally). Realistic sample geometry was considered ($a=30\,\mathrm{mm}$ and $L=8\,\mathrm{mm}$). The surface displacement along the z-direction, $u_z\left(r,z=0,t\right)$, is calculated and the results are used to generate the numerical simulations for the PM signal. This process is described below.

3.3 Photomechanical mirror

The pump-probe PM method uses one laser to irradiate the sample normal to its surface and a low-irradiance laser to probe the sample's surface deformation. This is performed by measuring the on-axis intensity variation of the central portion of the probe beam reflected off of the sample surface at the far-field. The symmetrical inward/outward displacement of the fluid surface converges/diverges, respectively, the probe beam at the detector, increasing/diminishing the signal at the detector. The experimental apparatuses used in this work are illustrated in Fig. 3.1 for continuous and pulsed excitation.

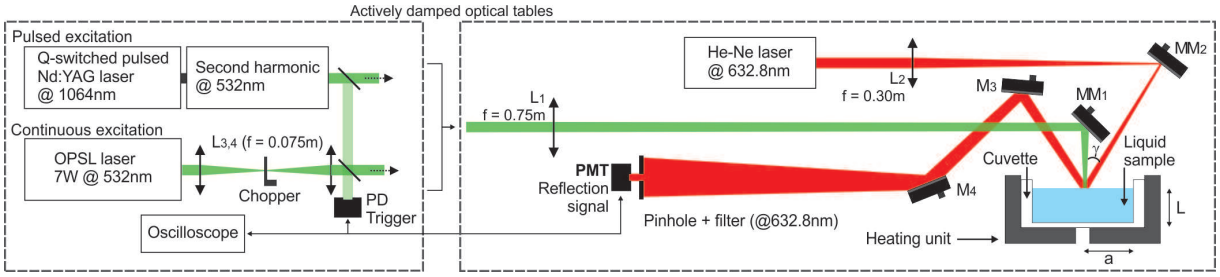

Figure 3.1: Experimental diagram for photomechanical mirror measurements. Continuous or pulsed excitation beams were focused on the sample surface. A continuous laser was arranged almost collinear to the excitation beam to probe the deformation of the liquid surface. The intensity variation of the probe beam center after reflection was detected by a pinhole-laser line filter-photomultiplier (PMT) assembly in the far-field. A digital oscilloscope triggered by the photodiode (PD) recorded the data at a repetition frequency of 10 Hz for the pulsed experiments and 100 Hz for the continuous. The apparatus was set up in separated actively damped optical tables to eliminate mechanical vibration on the liquid surface. The temperature of the samples was (298.15 ± 0.01) K. A detailed description of the experiment is presented in the Section 3.4.

The deformation of the sample surface produces a phase shift to the reflected probe beam given by [28]

$$\Phi_{\mathrm{PM}}\left(r,t\right) = \frac{4\pi}{\lambda_p} u_z\left(r, z=0, t\right), \tag{3.12}$$

where λ_{p} is the probe beam wavelength. Considering only the center of the probe beam spot at the detector plane in the far-field region, and using Fresnel diffraction theory, the relative intensity signal $S\left(t\right)$ results in [28]

$$S\left(t\right) = \left| \int_0^\infty \frac{2r}{\omega_{1\mathrm{p}}^2} \exp\left[-\left(1+iV\right) \frac{r^2}{\omega_{1\mathrm{p}}^2} - i\,\Phi_{\mathrm{PM}}(r,t) \right] \mathrm{d}r \right|^2 , \tag{3.13}$$

where $V = z_{1\mathrm{p}}/z_{\mathrm{cp}} + z_{\mathrm{cp}}[(z_{1\mathrm{p}}/z_{\mathrm{cp}})^2+1]/z_{2\mathrm{p}}$, z_{cp} is the confocal distance of the probe beam, $z_{1\mathrm{p}}$ is the distance from the probe beam waist to the sample, $z_{2\mathrm{p}}$ is the distance between the sample and the detector, and $\omega_{1\mathrm{p}}$ the radius of the probe beam at the sample surface. Eq. 3.13 can be evaluated numerically. The calculation of $S\left(t\right)$ requires the determination of $u_z\left(r, z=0, t\right)$ considering all the effects of the radiation forces in the liquid.

Several calculated surface deformation and PM transient signals in Figs. 3.2 (cw) and 3.3 (pulsed) illustrate the effects of density, dynamic viscosity and surface tension on $u_z\left(r, z=0, t\right)$ and $S\left(t\right)$. All the other parameters used in the simulations are those of water (Table 3.1). Figs. 3.2 and 3.3 (a)-(c) present the actual motion of the liquid surface at a fixed time considering different physical properties. Under continuous excitation, Fig. 3.2, the liquid surface rises with time reaching a maximum deformation of a few nanometers at the center of the excitation laser beam. Symmetrical waves propagate on the surface and also contribute to the convoluted intensity signal observed at the detector.

Table 3.1: Physical properties of the liquids used in the simulations [28,88–96].[a] Experimentally obtained (Anton-Paar, Density meter DMA5000). [b] Experimentally obtained (Brookfield, Rheometer DV-III). [c] Experimentally obtained (Atago, Digital Refractometer RX-5000, 589 nm).

Sample	Mass density kg m^{-3}	Dynamic viscosity cP	Surface tension mN m^{-1}	Refractive index
Ethanol	803.4	1.081	21.9	1.36
Ethylene glycol	1113.0	16.75	48.0	1.45
Nujol	864.5[a]	109.80[b]	32.0	1.46[c]
Water	998.2	0.893	72.0	1.33
0.053 wt% Brij	998.2	1.04 ± 0.06[b]	38 ± 2	1.33
0.01 wt% Brij	998.2	1.04 ± 0.06[b]	39 ± 2	1.33
0.005 wt% Brij	998.2	1.04 ± 0.06[b]	41 ± 1	1.33
0.001 wt% Brij	998.2	1.04 ± 0.06[b]	47.7 ± 0.9	1.33
0.0001 wt% Brij	998.2	1.04 ± 0.06[b]	57 ± 2	1.33
0.00001 wt% Brij	998.2	1.04 ± 0.06[b]	69 ± 3	1.33

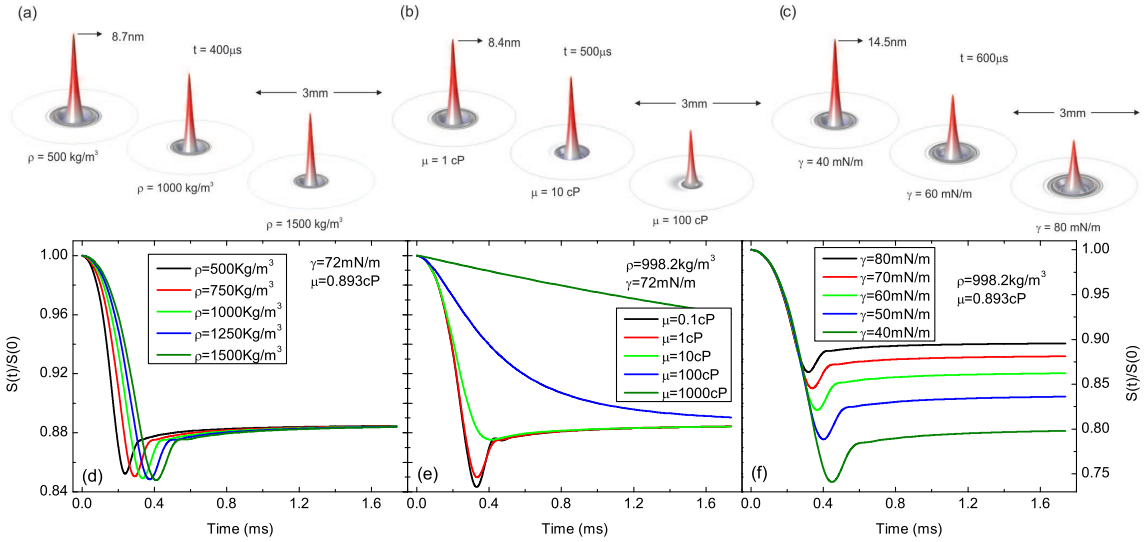

Figure 3.2: Evolution of liquid surface deformation under continuous excitation at fixed time varying (a) ρ–density, (b) μ–dynamic viscosity, and (c) γ–surface tension. The excitation beam radius and power were $\omega_e = 107\,\mu$m and $P_e = 2\,$W, respectively, $\omega_{1p} = 1264\,\mu$m, and $V = 27.5$. (d)-(f) show the corresponding PM transient signal calculated using Eq. 3.13, $S(t)/S(0)$.

When excited by a pulse, Fig. 3.3, a sharp peak appears on the surface of the liquid a few μs after irradiation and is rapidly dispersed. The probe beam senses the entire region affected by the excitation laser, and the complex reflection pattern of the probe beam just out of the sample propagates to the detector plane. The intensity variation measured at the center of the probe beam in the far-field has a convoluted contribution from all the surface waves created on the liquid.

Figures 3.2 and 3.3 (d)-(f) show the effect of these properties on the calculated

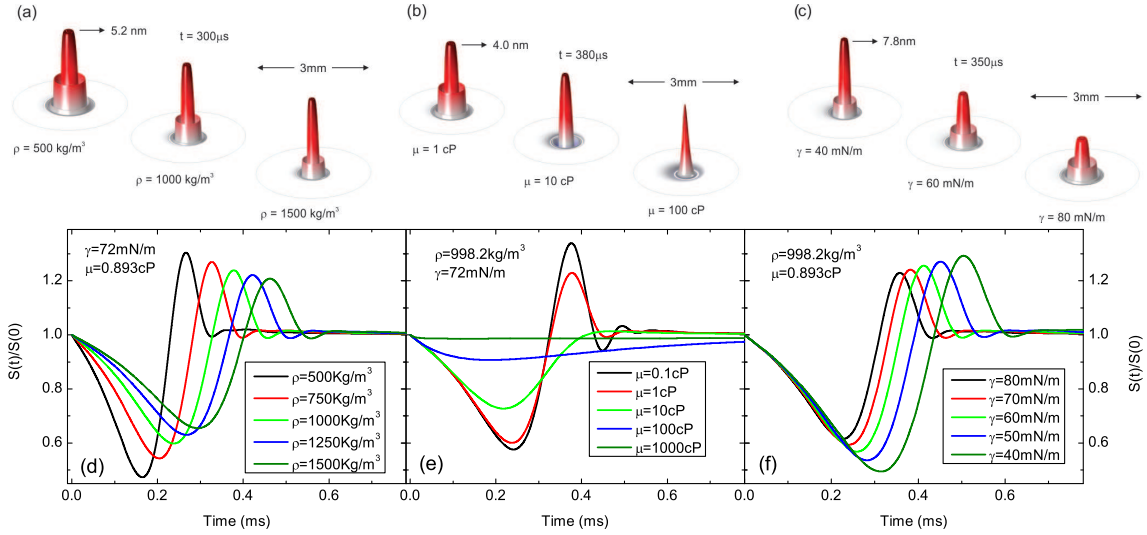

Figure 3.3: Evolution of liquid surface deformation under pulsed excitation at fixed time varying (a) ρ–density, (b) μ–dynamic viscosity, and (c) γ–surface tension. The excitation beam radius and energy were $\omega_e = 107\,\mu$m and $E_n = 1\,mJ$, respectively, $\omega_{1p} = 1264\,\mu$m, and $V = 27.5$. (d)-(f) show the corresponding PM transient signal calculated using Eq. 3.13, $S(t)/S(0)$.

PM transient signal. Higher density generates transients reaching the steady-state at longer times affecting slightly the amplitude signal under cw and pulsed excitations. A modification in dynamic viscosity alters the shape of the transient curves, mainly at short times. Although higher viscosity takes longer to achieve the steady-state it does not affect its final amplitude signal. Surface tension, on the other hand, affects the amplitude signal and its build-up time. The lower the surface tension, the stronger the amplitude signal.

3.4 Methods

Experimental diagram for photomechanical mirror measurements are described as follows: Continuous or pulsed laser excitations are provided by TEM_{00} beams with an optically pumped semiconductor laser (Coherent, Verdi G7, 532 nm) or a Q-switched pulsed Nd:YAG with second harmonic TEM_{00} laser operating at 532 nm (Quantel, Brilliant B, pulse width of 15 ns), respectively. The excitation beams were focused on the sample surface using a $f = 0.75$ m focal length lens (L_1). A 30 mW continuous TEM_{00} He-Ne laser at 632.8 nm (Melles Griot, Model 25-LHR-151-249), almost collinear to the excitation beam ($\gamma < 1°$), focused by lens L_2 ($f = 0.30$ m), was used to probe the deformation of the sample surface. The intensity variation of the probe beam center after reflection was detected by a pinhole-laser line filter-photomultiplier (PMT) assembly in a far field (approximately 6.8 m from the sample surface). The laser line filter is used to prevent the excitation laser beam and ambient light from being detected by the photomultiplier tube (Hamamatsu, Model R928). The PMT was biased with a high voltage power supply (Newport, Model 70706). A digital oscilloscope (Tektronix, Model DPO4102B) recorded

the data. Partial reflections from the excitation beams were used to trigger the oscilloscope by the photodiode PD (Newport, Model 818-BB-22) at a repetition frequency of 10 Hz for the pulsed experiments and 100 Hz for the continuous. A mechanical chopper (Thorlabs, Model MC2000) was used to modulate the continuous excitation. To eliminate mechanical vibration on the liquid surface, the excitation lasers, chopper and the motorized (Thorlabs, Model ZST213) alignment mirrors (MM_1 and MM_2) were placed in separated actively damped optical tables, as shown in the details (dashed lines). A heating unit and a temperature controller (Lakeshore, Model 340) were used to set the samples temperature to (298.15 ± 0.01) K . The excitation and probe beam radii were measured with a beam profiler (Thorlabs, Model BP104-UV) and a beam profile camera (Coherent, Model Lasercam HR). Laser energy and power were measured using a pyroelectric energy sensor (Thorlabs, Model ES120C) and a power meter (Spectra-Physics, Model 407A), respectively.

Samples with different physical properties were chosen for the experiments; Ethanol (99.9%), Nujol (99.5%), Ethylene glycol (99.5%), and aqueous solutions of 0.053 wt% to 0.00001 wt% Brij 35 [$CH_3(CH_2)_{11}(OCH_2CH_2)_{23}OH$, polyoxyethylene 23 lauryl ether]. Micellar solutions of Brij 35 were prepared by weighing the required amounts of Brij 35 in Milli-Q water. The samples were placed in a cylindrical quartz cuvette of radius $a = 30$ mm and $L = 8$ mm high. The sample temperature was (298.15 ± 0.01) K. For each sample, more than 100 transients were averaged and results for the photomechanical mirror signals under continuous and pulsed laser excitations at 532 nm are presented in Figs. 3.4 and 3.5. The transients show the intensity variation of the center of a continuous probe beam laser reflected off of the liquid surface measured at the photomultiplier tube (PMT) positioned in the far-field. Power and energy are listed in the figures. The laser beam dimensions and experimental parameters for PM setup are showed in Table 3.2.

Table 3.2: Experimental parameters for PM setup.

Parameters		Continuous excitation	Pulsed excitation
z_{1p}	mm	290	290
z_{2p}	m	6.8	6.8
z_{cp}	mm	11.0	11.0
V		27.5	27.5
ξ_p	ns		30
τ_p	ns		15
ω_{1p}	μm	1290	1317
ω_e	μm	107	133

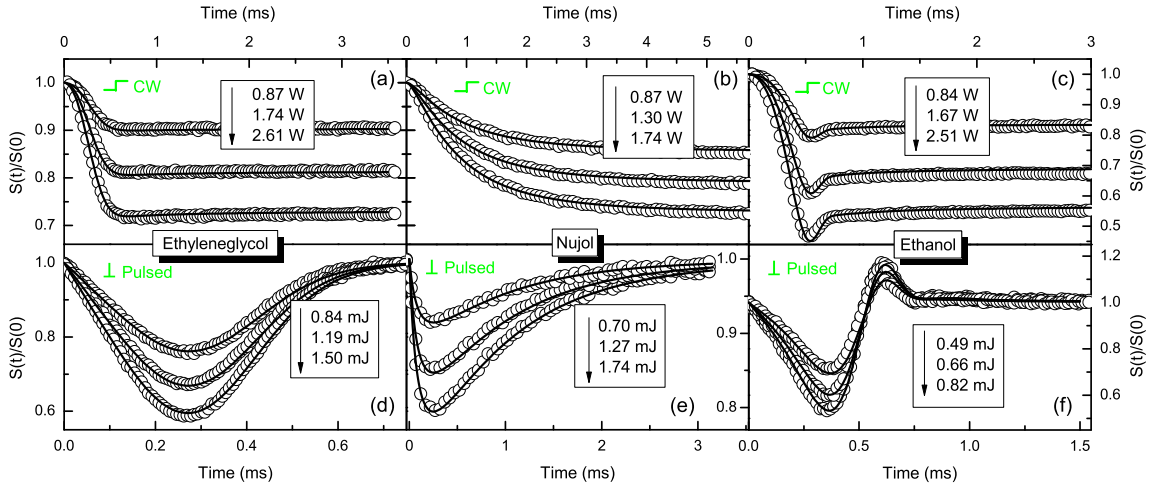

Figure 3.4: PM signal under continuous, (a)-(c), and pulsed, (d)-(f), laser excitations at 532 nm for Ethanol, Ethylene glycol, and Nujol. The transients show the intensity variation of the center of a continuous probe beam laser reflected off of the liquid surface measured at the photomultiplier tube (PMT) positioned in the far-field. Open symbols are experimental data and continuous lines represent the numerical calculations using $S\,(t)\,/S\,(0)$, in which $S\,(0)$ is the signal at $t = 0$. The error bars for the experimental data are smaller than 0.2%.

3.5 Results and discussion

Samples with different physical properties were chosen for the experiments; Ethanol (99.9%), Nujol (99.5%), Ethylene glycol (99.5%), and aqueous solutions of 0.053 wt% to 0.00001 wt% Brij 35 [$CH_3(CH_2)_{11}(OCH_2CH_2)_{23}OH$, polyoxyethylene 23 lauryl ether]. Micellar solutions of Brij 35 were prepared by weighing the required amounts of Brij 35 in Milli-Q water. The samples were placed in a cylindrical quartz cuvette of radius $a = 30$ mm and $L = 8$ mm high. The sample temperature was (298.15 ± 0.01) K. For each sample, more than 100 transients were averaged and results for the photomechanical mirror signals under continuous and pulsed laser excitations at 532 nm are presented in Figs. 3.4 and 3.5. The transients show the intensity variation of the center of a continuous probe beam laser reflected off of the liquid surface measured at the photomultiplier tube (PMT) positioned in the far-field. Power and energy are listed in the figures. The laser beam dimensions and experimental parameters for PM setup are showed in Supplementary Table 3.2.

Figure 3.4 shows PM transient signals under continuous, (a)-(c), and pulsed, (d)-(f), laser excitations for different powers and energy for Ethanol, Ethylene glycol, and Nujol. In the continuous irradiation experiments, the probe beam intensity decreases with time due to the elevation of the liquid. The surface distortion is always convex to the reflected probe beam and the corresponding signal shows a decrease in probe intensity past the pinhole at all times. As the viscosity of the samples has different order of magnitude, different shapes of transients are observed, as predicted by Fig. 3.2 (e). For Ethanol, the probe beam intensity decreases with time for a duration of less than 500 μs and, subse-

quently, a reduction in the signal towards a steady-state is observed. The same behavior are not observed for the other samples. For the pulsed excitation, the radiation force exerted in the liquid by the pulse is much shorter than the transient signal (pulse width was 15 ns). The PM sensor measures the surface wave propagating after the laser pulse. During pulsed irradiation, the surface first produces a convex column. For liquids with higher viscosity ($\mu > 10\,\mathrm{cP}$) the column return for the initial condition without creating a concave surface. However, for ethanol ($\mu < 10\,\mathrm{cP}$), the column subsequently collapses causing a concave surface perturbation to the probe beam. This behavior corresponds to the probe laser power initially decreasing then increasing past the pinhole. The behavior observed in the experimental data also can be ascertained by the numerical simulations, as described in Fig. 3.3 (e).

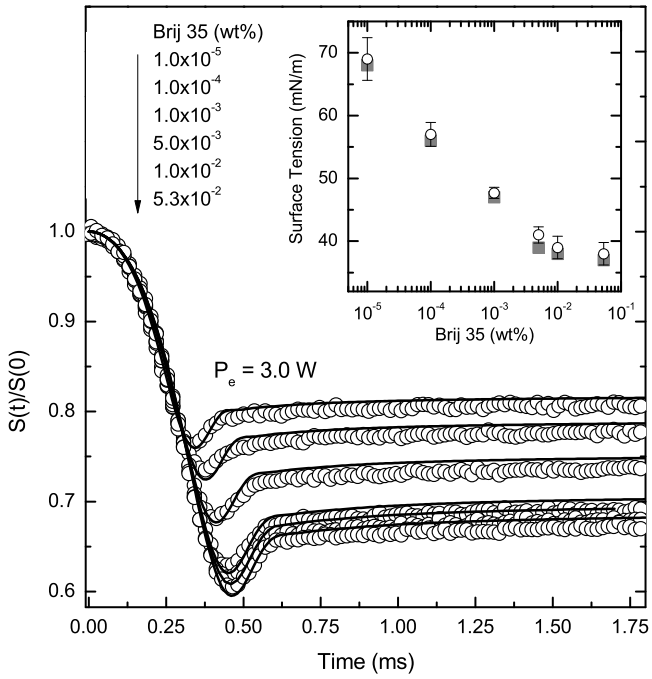

Figure 3.5: PM signal under continuous laser excitation at 532 nm for aqueous micellar solutions of Brij 35. Open symbols are experimental data and continuous lines represent the numerical calculations using $S(t)/S(0)$. Inset shows the surface tension obtained from all numerical calculations (gray squares) and steady-state fits (open circles).

Continuous lines in Figs. 3.4 show the calculated PM signals. The numerical predictions are in excellent agreement for both the continuous and pulsed excitation transients. In fact, it shows quantitatively that the effects of radiation forces in liquids can be fully described by Eq. 3.8. The physical properties of the samples used to calculate the PM signals are listed in Supplementary Table 3.1.

Figure 3.5 shows the effect of micellar solutions of Brij 35 on the surface tension of water under continuous excitation. The pattern shown on the transient curves by the addition of Brij resemble that presented in Figs. 3.2 (f) for different surface tensions. This is, in fact, the effect that the Brij has on water; a reduction of surface tension

with increasing micellar content, as presented in the inset. The continuous lines are the calculated PM signals using the parameters listed in Table 3.1. The only parameter susceptible to changes in the micellar solutions was the surface tension. It presented a value close to that for pure water for very low content of Brij and decreased substantially with increasing concentration of Brij.

The surface tension of the aqueous solutions can be analytically obtained from steady-state analysis. As for the air-liquid interface, the radiation pressure is compensated by the gravity and the Laplace force - the normal component of the interfacial tension applied to the curved interface [97]. It is considered that the continuous light is normally incident to the air-liquid interface at $z = 0$ from the air to the liquid filling the half space of $z < 0$. The surface displacement $u(\vec{r})$ under the light radiation is given by the following equation:

$$-\gamma\nabla^2 u(\vec{r}) + \rho g u(\vec{r}) = p(\vec{r}). \tag{3.14}$$

Here, γ is the surface tension and the pressure $p(\vec{r})$ for a cw Gaussian laser beam is

$$p(r) = -\frac{4P_{\mathrm{e}}}{c\pi\omega_{\mathrm{e}}^2}\left(\frac{n-1}{n+1}\right)\mathrm{e}^{-\frac{2r^2}{\omega_e^2}}. \tag{3.15}$$

Equation 3.14 can be solved using Hankel integral transform as

$$u(r) = \frac{P_{\mathrm{e}}}{c\pi}\left(\frac{n-1}{n+1}\right)\int_0^\infty \frac{\mathrm{e}^{-\frac{1}{8}\alpha^2\omega_{\mathrm{e}}^2}}{\gamma\alpha^2+\rho g}J_0(\alpha r)\alpha \mathrm{d}\alpha. \tag{3.16}$$

$J_n(x)$ is the Bessel Function of the first kind. The time-independent surface displacement can be used in the phase shift expression, Eq. 3.12, to calculate the signal, Eq. 3.13. From regression analysis, the surface tension of the liquid can be retrieved from steady-state signal. The results are presented in the inset of Fig. 3.5 and are in good agreement with the ones obtained using the time-dependent signal calculated numerically.

In an attempt to replicate the findings reported by Zhang and coauthors [83], we have performed experiments on water in air using unfocused excitation laser beam. We used a large container of water, as described in Fig. 3.6, and large excitation beam radius. The experimental parameters for these measurements are described in the caption of Fig. 3.6. These parameters reproduce the exact conditions on which the fluid would be put to motion during laser excitation and a cavitation should be seen on the water surface due to Abraham momentum transfer as predicted by Zhang and coauthors [83]. The authors state that neither the Abraham nor the Minkowski momentum is fundamental. Instead, they would emerge depending on the fluid-mechanical response of the medium to the light. With no motion, Minkowski momentum emerges; otherwise, Abraham momentum appears.

Fig. 3.6 shows PM signals for two different excitation powers. The transients are

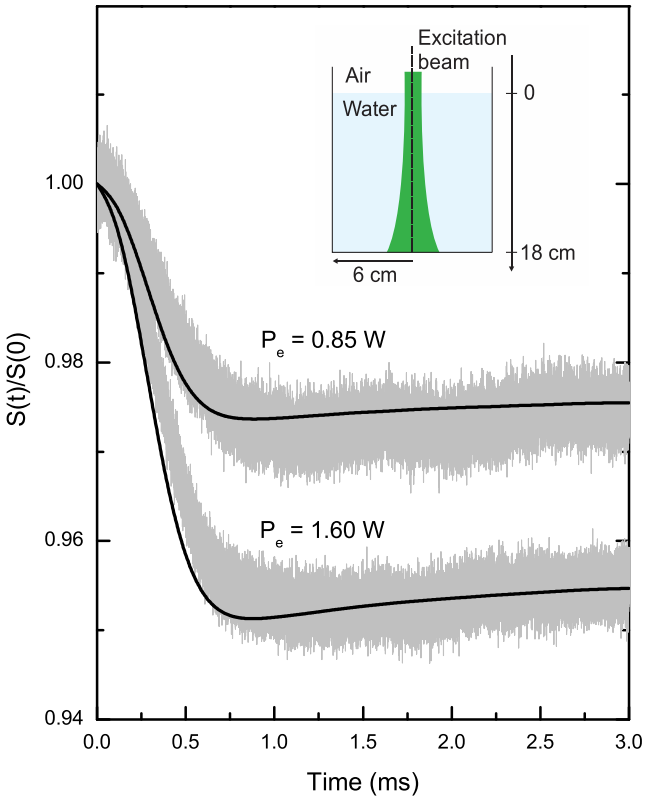

Figure 3.6: PM signal under continuous laser excitation at 532 nm for water. Inset shows the sample dimensions. The excitation laser beam is diverging inside the samples following the equation $\omega(z) = \omega_{\mathrm{e}}\sqrt{[1 + (z - z_{1\mathrm{e}})^2/z_{\mathrm{ce}}^2]}$ with $\omega_{\mathrm{e}} = 84\mu$m, $z_{1\mathrm{e}} = 0.21$ m, and $z_{\mathrm{ce}} = 42$ mm. The probe beam experimental parameters were: $\omega_{1\mathrm{p}} = 1600\,\mu$m, $z_{2\mathrm{p}} = 6.8$ m, and $V = 30.7$.

the opposite as predicted by the authors. We can see a diverging signal that is, in fact, due to an elevation of the fluid surface. We have also performed the experiments using several different experimental parameters as well as different containers of water with different volumes. In all the tests (not shown here), the transient signal resembles the one presented in Fig. 3.6, i.e., an elevation of the surface of water during laser excitation. Additionally, the theoretical predictions are in very good agreement for all the experimental transients, as shown by the continuous lines in Fig. 3.6. For the numerical calculations, we have considered the z-dependence on the excitation beam radius, $\omega(z)$, in the expressions leading to the intensity signal, Eq. 3.13. For this, addition contribution to the volume electrostriction force ($f_{z,\mathrm{V}}$) appears due to the z-dependence on the excitation beam radius. This contribution is written as

$$f_{z,\mathrm{V}} = \frac{1}{2}\varepsilon_0 \frac{\partial}{\partial z}\left[\rho\left(\frac{\partial \varepsilon_\mathrm{r}}{\partial \rho}\right)_T \left\langle E_\parallel \right\rangle^2\right]. \tag{3.17}$$

We emphasize that the PM configuration is very sensitive to very small phase shifts, which leads no doubt on the transient signals observed in our experiments. These results show that the overall effects observed are always an outward expansion of the fluid surface. For comparison, we tried to verify the findings of the authors [83] by projecting the excitation laser beam on the wall and taking pictures at different exposure times. The beam diameter remained almost constant during laser excitation. This indicates that such a small phase shift could not be precisely measured using their experimental approach. We believe the PM method described here to be superior.

3.6 Conclusion

In conclusion, we have experimentally demonstrated the effect of radiation forces in liquids with different physical properties. The numerical simulations are in excellent agreement with our experimental results. The expression used for the imparted pressure on the surface of the liquid from the Helmholtz force density, Eq. 3.3, has the same form as that using Minkowski momentum. Different experimental parameters and liquid volumes were tested and the results are all in agreement with the present theoretical description of radiation forces. Although the experiments performed here are not capable of discriminating between these two contributions, we have assessed that for all these different materials and experimental configurations, Minkowski momentum transfer still holds and describes the surface deformation observed. However, Minkowski formulation could be as well regarded as the total momentum in the system; a sum of the momentum which propagates with the electromagnetic wave, the Abraham momentum, and that which is deposited locally in the material.

Chapter 4

General Conclusion and Future Perspective

The advances recently made in the development of the photothermal methods have opened a new way to look into localized effects created by laser excitation. In summary, we have shown that the applicability of the photothermal/photomechanical mirror method can be extended to visualize laser induced thermoelastic waves in metals generated by light absorption and surface deformations at liquid/air interface induced solely by electromagnetic momentum transfer between light and matter.

Using the photothermal mirror method, we were able to visualize laser induced thermoelastic waves generated locally and propagating within metals. Heat deposition by the pulse launches bulk and surface waves and generates large surface swelling of the sample under the excitation area. Numerical solutions of the coupled heat diffusion and thermoelastic equations and the experimental results were in complete agreement and represented both the thermal diffusion of large amplitudes, long-lasting outward bulge, and the released elastic waves. The velocity field calculations show the moving wavefronts of various types of elastic waves inside the samples. The launched elastic waves propagate on the surface and within the solids generating convoluted photothermal mirror signals following the thermo-mechanical properties of the sample. The elastic waves are predicted by numerical solution of the thermoelastic equation and have properties closely related to the familiar elastic waves created by an isotropic point-expansion source on the surface of solids. The influence of sample thickness on the surface deformation and photothermal mirror signal was studied in detail.

Using the photomechanical mirror approach, we induced nanometer-scale surface deformations by exploiting momentum conservation of the interaction between the laser light and dielectric liquids, mitigating thermal effects. The method was employed for a systematic study to assess quantitatively the effect of radiation force at the air-liquid interface of fluids with different physical properties. Numerical simulations considering the imparted pressure on the surface of the liquid from the Helmholtz force density were in a good agreement with the experiments.

We foresee further potential use of the photothermal/photomechanical methods for applications in materials characterization, as light-induced elastic waves are ultimately connected to the medium local optical and viscoelastic properties. In addition, volume and surface momentum-driven elastic waves could be decoupled by using different excitation beam geometry, for instance, by focusing or defocusing the excitation beam along the sample thickness. This would allow for maximizing or minimizing the effects of either radiation pressure imparted on the surface or electrostriction volume forces in the materials allowing us to access the effects dependent on the optical force distribution.

Many studies can be done considering the techniques presented in this work. Thermoelastic waves induced in thinner samples by photothermal mirror technique has a good potential on the study of thermal and mechanical properties of thin films. The propagation of induced waves on the surface of metals can also be studied considering the coupling of a metal with different liquids. Preliminary studies show a dependence of the surrounding fluid on the waves that propagate in the system and consequently on the obtained photothermal mirror signal.

The use of the photomechanical mirror technique, in addition to the important contribution to the quantitative description of forces acting at the interface between dielectric fluids and air, is still efficient in the physical characterization of different liquids, so that studies considering temperature variations and different pressure conditions still deserve attention.

Appendix A

Permission letters from publishers

The contents of this appendix are the permission letters from the American Institute of Physics (AIP) and from Springer Nature Publishing Group guaranteeing the legal usage from the articles in this thesis. The letters are in the format of an email answer sent from the publishers above mentioned.

A.1 Permission Letter from Applied Physics Letters

RE: Letter Permission Appl. Phys. Lett. 109, 191908 (2016)

AIPRights Permissions <Rights@aip.org>

qui 21/12/2017 17:38

Para:Otávio Augusto <oacapeloto@hotmail.com>;

Dear Dr. Capeloto:

You are permitted to include your published article or material from it in your thesis, provided you also include a credit line referencing the original publication.

Our preferred format is (please fill in the citation information):

"Reproduced from [FULL CITATION], with the permission of AIP Publishing."

Please let us know if you have any questions.

Sincerely,
Susann Brailey
Manager, Rights & Permissions

AIP Publishing
1305 Walt Whitman Road | Suite 300 | Melville NY 11747-4300 | USA
t +1.516.576.2268
rights@aip.org | [publishing.aip.org]publishing.aip.org
Follow us: Facebook | Twitter | LinkedIn

From: Otávio Augusto [mailto:oacapeloto@hotmail.com]
Sent: Tuesday, December 19, 2017 7:49 AM
To: AIPRights Permissions <Rights@aip.org>
Subject: Letter Permission Appl. Phys. Lett. 109, 191908 (2016)

Dear Editor,

I recently published a paper "Generation and detection of thermoelastic waves in metals by a photothermal mirror method - Appl. Phys. Lett. **109**, 191908 (2016); https://doi.org/10.1063/1.4967530" at the Applied Physics Letters. This work is the foundation of my Ph.D. thesis and it will be published and cataloged in the university repository, in a totally non-commercial form.

Since the university requires a formal permission from AIP Publishing Group, I kindly ask you if it is possible to reproduce partially or fully the mentioned work as an academic dissertation/thesis.

Besides, I also want to know if there is a proper way to acknowledge the publisher in the thesis.

Thank you in advance,

A.2 Permission Letter from Scientific Reports

RE: Permission Letter Scientific Reports doi:10.1038/srep20515

Journalpermissions <journalpermissions@springernature.com>

qui 21/12/2017 14:12

Para:oacapeloto@hotmail.com <oacapeloto@hotmail.com>;

Cc:SciRep.Admin <SciRep.Admin@nature.com>;

Dear Otávio,

Thank you for your email. This work is licensed under a Creative Commons Attribution 4.0 International License which allows reuse of the material without permission provided that you clearly acknowledge the original publication. To view a copy of this license, visit http://creativecommons.org/licenses/by/4.0/

Kind Regards,

Claire Harper (née Smith)
Journal Permissions Manager

SpringerNature
The Campus, 4 Crinan Street, London N1 9XW, United Kingdom
T +44 (0) 207 014 4129

From: Otávio Augusto [mailto:oacapeloto@hotmail.com]
Sent: 19 December 2017 12:29
To: reports, scientific
Subject: Permission Letter Scientific Reports doi:10.1038/srep20515

Dear Dr. Suzanne Farley

I recently published a paper “Quantitative assessment of radiation force effect at the dielectric air-liquid interface - *Scientific Reports* **6**, Article number: 20515 (2016)” at the Scientific Reports. This work is the foundation of my Ph.D. thesis and it will be published and cataloged in the university repository, in a total non commercial form.
Since the university requires a formal permission from Springer Nature Group, I kindly ask you if it is possible to reproduce partially or fully the mentioned work as an academic dissertation/thesis.
Besides I also want to know if there is a proper way to acknowledge the publisher in the thesis.

Thank you in advance,

Best Regards

M.Sc. Otávio Augusto Capeloto

Appendix B

Electromagnetic forces at a dielectric fluid

The interaction of electromagnetic waves with a certain material can result different physical phenomena such as heating [23], ionization [98], chemical reactions [99], and other. Not less important, a material subject to electromagnetic waves also feels a force due to such waves [84].

If the medium is at rest, subject to an variable electromagnetic field, the force per unit volume $\vec{f}$ that the medium feels can be calculated using the relation of force with the stress tensor σ_{ik} [84]

$$f_i = \sum_k \frac{\partial \sigma_{ik}}{\partial x_k} - \frac{\partial G_i}{\partial t}. \tag{B.1}$$

For a dielectric fluid in the absence of free charge and current, the momentum density is $\vec{G} = \vec{E} \times \vec{H}/c^2$, where $\vec{E}$ and $\vec{H}$ describe the electric and magnetic fields, and c is the speed of light.

The stress tensor σ_{ik} is the momentum flux density [84], e. g., is the sum of the momentum of electromagnetic field and the matter. The second term is the rate of change of the field momentum per unit volume.

For an electromagnetic field, the stress tensor σ_{ik} has the contribution of an electric part and a magnetic part. The electric and magnetic components of the stress tensor can be obtained from thermodynamics relations between electric and magnetic fields with the medium and a well explanation can be found in Ref. [84][1]. The electromagnetic stress tensor is written as [84]

[1] Other formulations for electromagnetic tensor are proposed by many authors resulting on different forms for the expression of the force that acts on the dielectric. As further reading for more information, consult Refs. [100] and [101].

$$\sigma_{ik} = -P_0(\rho,T)\delta_{ik} \;-\; \frac{1}{2}\varepsilon_0 E^2\left[\varepsilon_\mathrm{r} - \rho\left(\frac{\partial\varepsilon_\mathrm{r}}{\partial\rho}\right)_T\right]\delta_{ik} + \varepsilon_\mathrm{r}\varepsilon_0 E_i E_k \qquad \text{(B.2)}$$
$$- \;\frac{1}{2}\mu_0 H^2\left[\mu_\mathrm{r} - \rho\left(\frac{\partial\mu_\mathrm{r}}{\partial\rho}\right)_T\right]\delta_{ik} + \mu_\mathrm{r}\mu_0 H_i H_k.$$

Here, P_0 is the constant pressure at interface in absence of radiation forces, ε_0 the electric permittivity of vacuum, ε_r the relative electric permittivity, μ_0 the magnetic permeability of vacuum, μ_r the relative magnetic permeability, T the temperature, and ρ tha mass density.

The expression of the force f_i can be calculated replacing Eq. B.2 in B.1 to obtain

$$f_i = -\frac{\partial P_0}{\partial x_k}\delta_{ik} \;-\; \frac{\partial}{\partial x_k}\left(\frac{1}{2}\varepsilon_\mathrm{r}\varepsilon_0 E^2\right)\delta_{ik} + \frac{\partial}{\partial x_k}\left[\frac{1}{2}\varepsilon_0 E^2\rho\left(\frac{\partial\varepsilon_\mathrm{r}}{\partial\rho}\right)_T\right]\delta_{ik} + \frac{\partial}{\partial x_k}\left(\varepsilon_\mathrm{r}\varepsilon_0 E_i E_k\right)$$
$$- \;\frac{\partial}{\partial x_k}\left(\frac{1}{2}\mu_\mathrm{r}\mu_0 H^2\right)\delta_{ik} + \frac{\partial}{\partial x_k}\left[\frac{1}{2}\mu_0 E^2\rho\left(\frac{\partial\mu_\mathrm{r}}{\partial\rho}\right)_T\right]\delta_{ik} + \frac{\partial}{\partial x_k}\left(\mu_\mathrm{r}\mu_0 H_i H_k\right)$$
$$- \;\frac{\partial}{\partial t}\frac{\vec{E}\times\vec{H}}{c^2}\,, \qquad \text{(B.3)}$$

where the derivatives $\frac{\partial}{\partial x_k}\left(\frac{1}{2}\varpi\Lambda^2\right)\delta_{ik}$, and $\frac{\partial}{\partial x_k}\left(\varpi\Lambda_i\Lambda_k\right)$ is replaced by

$$\frac{\partial}{\partial x_k}\left(\frac{1}{2}\varpi\Lambda^2\right)\delta_{ik} = \varpi\Lambda_k\left(\frac{\partial\Lambda_k}{\partial x_k}\right)\delta_{ik} + \frac{1}{2}\Lambda^2\left(\frac{\partial\varpi}{\partial x_k}\right)\delta_{ik}\,, \qquad \text{(B.4)}$$

and

$$\frac{\partial}{\partial x_k}\left(\varpi\Lambda_i\Lambda_k\right) = \Lambda_i\left[\frac{\partial\left(\varpi\Lambda_k\right)}{\partial x_k}\right] + \varpi\Lambda_k\left(\frac{\partial\Lambda_i}{\partial x_k}\right)\,, \qquad \text{(B.5)}$$

with $\varpi = \varepsilon_\mathrm{r}\varepsilon_0$, $\Lambda = E$ for electric field and $\varpi = \mu_\mathrm{r}\mu_0$, $\Lambda = H$ for magnetic field. Considering the fact that $\delta_{ik} = 0$ if $i \neq k$ and $\delta_{ik} = 1$ if $i = k$, the Eq. B.3 is rewritten as

$$f_i = \;-\; \varepsilon_\mathrm{r}\varepsilon_0 E_k\left(\frac{\partial E_k}{\partial x_i}\right) - \frac{1}{2}\varepsilon_0 E^2\left(\frac{\partial\varepsilon_\mathrm{r}}{\partial x_i}\right) + \frac{\partial}{\partial x_i}\left[\frac{1}{2}\varepsilon_0 E^2\rho\left(\frac{\partial\varepsilon_\mathrm{r}}{\partial\rho}\right)_T\right]$$
$$+ \;E_i\left[\frac{\partial\left(\varepsilon_\mathrm{r}\varepsilon_0 E_k\right)}{\partial x_k}\right] + \varepsilon_\mathrm{r}\varepsilon_0 E_k\left(\frac{\partial E_i}{\partial x_k}\right)$$
$$- \;\mu_\mathrm{r}\mu_0 H_k\left(\frac{\partial H_k}{\partial x_i}\right) - \frac{1}{2}\mu_0 H^2\left(\frac{\partial\mu_\mathrm{r}}{\partial x_i}\right) + \frac{\partial}{\partial x_i}\left[\frac{1}{2}\mu_0 H^2\rho\left(\frac{\partial\mu_\mathrm{r}}{\partial\rho}\right)_T\right]$$
$$+ \;H_i\left[\frac{\partial\left(\mu_\mathrm{r}\mu_0 H_k\right)}{\partial x_k}\right] + \mu_\mathrm{r}\mu_0 H_k\left(\frac{\partial H_i}{\partial x_k}\right) - \frac{\partial}{\partial t}\frac{\vec{E}\times\vec{H}}{c^2}\,,$$

or

$$
\begin{aligned}
f_i = & - \frac{1}{2}\varepsilon_0 E^2 \left(\frac{\partial \varepsilon_\mathrm{r}}{\partial x_i}\right) + \frac{\partial}{\partial x_i}\left[\frac{1}{2}\varepsilon_0 E^2 \rho \left(\frac{\partial \varepsilon_\mathrm{r}}{\partial \rho}\right)_T\right] + \varepsilon_\mathrm{r}\varepsilon_0 E_k \left(\frac{\partial E_i}{\partial x_k} - \frac{\partial E_k}{\partial x_i}\right) \\
& - \frac{1}{2}\mu_0 H^2 \left(\frac{\partial \mu_\mathrm{r}}{\partial x_i}\right) + \frac{\partial}{\partial x_i}\left[\frac{1}{2}\mu_0 H^2 \rho \left(\frac{\partial \mu_\mathrm{r}}{\partial \rho}\right)_T\right] + \mu_\mathrm{r}\mu_0 H_k \left(\frac{\partial H_i}{\partial x_k} - \frac{\partial H_k}{\partial x_i}\right) \\
& + \varepsilon_0 E_i \left[\frac{\partial\left(\varepsilon_\mathrm{r} E_k\right)}{\partial x_k}\right] + \mu_0 H_i \left[\frac{\partial\left(\mu_\mathrm{r} H_k\right)}{\partial x_k}\right] - \frac{\partial}{\partial t}\frac{\vec{E}\times\vec{H}}{c^2}\,. \qquad \text{(B.6)}
\end{aligned}
$$

Employing the vectorial relation [102]

$$
-\Lambda_k \left(\frac{\partial \Lambda_i}{\partial x_k} - \frac{\partial \Lambda_k}{\partial x_i}\right) = \vec{\Lambda}\times\nabla\times\vec{\Lambda}, \qquad \text{(B.7)}
$$

the force expression is written in vectorial form,

$$
\begin{aligned}
\vec{f} = & - \frac{1}{2}\varepsilon_0 \langle E\rangle^2 \nabla\varepsilon_\mathrm{r} + \nabla\left[\frac{1}{2}\varepsilon_0\langle E\rangle^2\rho\left(\frac{\partial\varepsilon_\mathrm{r}}{\partial\rho}\right)_T\right] - \varepsilon_\mathrm{r}\varepsilon_0\vec{E}\times\nabla\times\vec{E} \\
& - \frac{1}{2}\mu_0 \langle H\rangle^2 \nabla\mu_\mathrm{r} + \nabla\left[\frac{1}{2}\mu_0\langle H\rangle^2\rho\left(\frac{\partial\mu_\mathrm{r}}{\partial\rho}\right)_T\right] - \mu_\mathrm{r}\mu_0\vec{H}\times\nabla\times\vec{H} \\
& + \vec{E}\cdot\nabla\cdot\left(\varepsilon_\mathrm{r}\varepsilon_0\vec{E}\right) + \vec{H}\cdot\nabla\cdot\left(\mu_\mathrm{r}\mu_0\vec{H}\right) - \frac{\partial}{\partial t}\frac{\vec{E}\times\vec{H}}{c^2}\,. \qquad \text{(B.8)}
\end{aligned}
$$

Where $\langle E\rangle^2$, and $\langle H\rangle^2$ are the mean quadratic fields [102]. Here, the constitutive linear relations $\vec{D} = \varepsilon_\mathrm{r}\varepsilon_0\vec{E}$ and $\vec{B} = \mu_\mathrm{r}\mu_0\vec{H}$ are used to write

$$
\begin{aligned}
\vec{f} = & - \frac{1}{2}\varepsilon_0 \langle E\rangle^2 \nabla\varepsilon_\mathrm{r} + \nabla\left[\frac{1}{2}\varepsilon_0\langle E\rangle^2\rho\left(\frac{\partial\varepsilon_\mathrm{r}}{\partial\rho}\right)_T\right] - \varepsilon_\mathrm{r}\varepsilon_0\vec{E}\times\nabla\times\vec{E} \\
& - \frac{1}{2}\mu_0 \langle H\rangle^2 \nabla\mu_\mathrm{r} + \nabla\left[\frac{1}{2}\mu_0\langle H\rangle^2\rho\left(\frac{\partial\mu_\mathrm{r}}{\partial\rho}\right)_T\right] - \mu_\mathrm{r}\mu_0\vec{H}\times\nabla\times\vec{H} \\
& + \vec{E}\cdot\left(\nabla\cdot\vec{D}\right) + \vec{H}\cdot\left(\nabla\cdot\vec{B}\right) - \frac{\partial}{\partial t}\frac{\vec{E}\times\vec{H}}{c^2}\,, \qquad \text{(B.9)}
\end{aligned}
$$

where $\vec{D}$ is the Electric Displacement field and $\vec{B}$ is the Magnetic flux density.

Considering the Faraday's law and Ampère's law with no free charges and no free current, the vectorial force per unit volume that the fluid is subject is written as

$$
\begin{aligned}
\vec{f} = & - \frac{1}{2}\varepsilon_0 \langle E\rangle^2 \nabla\varepsilon_\mathrm{r} - \frac{1}{2}\mu_0 \langle H\rangle^2 \nabla\mu_\mathrm{r} + \nabla\left[\frac{1}{2}\varepsilon_0\langle E\rangle^2\rho\left(\frac{\partial\varepsilon_\mathrm{r}}{\partial\rho}\right)_T\right] \\
& + \nabla\left[\frac{1}{2}\mu_0\langle H\rangle^2\rho\left(\frac{\partial\mu_\mathrm{r}}{\partial\rho}\right)_T\right] - \frac{\varepsilon_\mathrm{r}-1}{c^2}\frac{\partial}{\partial t}\left(\vec{E}\times\vec{H}\right)\,. \qquad \text{(B.10)}
\end{aligned}
$$

In a dielectric fluid, as it has been considered in all the work, the relative magnetic

permeability μ_r can be considered $\mu_r = 1$. Hence Eq. B.10 is replaced by [28]

$$\vec{f} = -\frac{1}{2}\varepsilon_0 \langle E \rangle^2 \nabla \varepsilon_r + \frac{1}{2}\varepsilon_0 \nabla \left[\langle E \rangle^2 \rho \left(\frac{\partial \varepsilon_r}{\partial \rho} \right)_T \right] - \frac{\varepsilon_r - 1}{c^2} \frac{\partial}{\partial t} \left(\vec{E} \times \vec{H} \right) . \tag{B.11}$$

The first term in Eq. B.11 appears in Minkowski and Abraham energy-momentum tensor formulations. This force acts where relative permittivity presents spatial variation. The second term accounts for the deformation (electrostriction) caused by the field inhomogeneity. The last term is known as the Abraham force density. This term is supposed to average to zero at optical frequencies and can be neglected in our model. In our experiments, the Abraham and Minkowski expression for the force are identical. This fact makes the Minkowski tensor, with the inclusion of the electrostriction term, an attractive formulation for experiments in optics [16, 85]. Thus, Eq. B.11 reduces to the Helmholtz force [84, 86].

References

[1] Požar, T. & Možina, J. Measurement of elastic waves induced by the reflection of light. *Phys. Rev. Lett.* **111**, 25 (2013).

[2] Royer, D. & Dieulesaint, E. Elastic waves in solids. Springer (Springer-Verlag Berlin Heidelberg, 2000).

[3] Scruby, C. B. & Drain, L. E. Laser ultrasonics techniques and applications (CRC Press, 1990).

[4] Gusev, V. Ė. & Karabutov, A. A. Laser Optoacoustics. (American Institute of Physics, 1993).

[5] Davies, S. J., Edwards, C., Taylor, G. S. & Palmer, S. B. Laser-Generated Ultrasound - Its Properties, Mechanisms and Multifarious Applications. *J. Phys. D. Appl. Phys.* **26**, 329-348 (1993).

[6] Hutchins, D. a. Mechanisms of pulsed photoacoustic generation. *Can. J. Phys.* **64**, 1247-1264 (1986).

[7] McDonald, F. A. Practical quantitative theory of photoacoustic pulse generation. *Appl. Phys. Lett.* **54**, 1504-1506 (1989).

[8] Dewhurst, R. J., Hutchins, D. A., Palmer, S. B. & Scruby, C. B. Quantitative measurements of laser-generated acoustic waveforms. *J. Appl. Phys.* **53**, 4064-4071 (1982).

[9] Spicer, J. B. & Hurley, D. H. Epicentral and near epicenter surface displacements on pulsed laser irradiated metallic surfaces. *Appl. Phys. Lett.* **68**, 3561-3563 (1996).

[10] Požar, T. Babnik, A. & Možina, J. From laser ultrasonics to optical manipulation. *Opt. Express* **23**, 7978 (2015).

[11] Pfeifer, R. N. C., Nieminen, T. A., Heckenberg, N. R. & Rubinsztein-Dunlop, H. Colloquium: Momentum of an electromagnetic wave in dielectric media. *Rev. Mod. Phys.* **79**, 1197-1216 (2007).

[12] Milonni, P. W. & Boyd, R. W. Momentum of light in a dielectric medium. *Adv. Opt. Photon.* **2**, 519-553 (2010).

[13] Barnett, S. M. & Loudon, R. The enigma of optical momentum in a medium. *Philos. Trans. R. Soc. London Ser. A* **368**, 927-939 (2010).

[14] Kemp, B. A. Resolution of the Abraham-Minkowski debate: Implications for the electromagnetic wave theory of light in matter. *J. Appl. Phys.* **109**, 111101 (2011).

[15] Baxter, C. & Loudon, R. Radiation pressure and photon momentum in dielectrics. *J. Mod. Opt.* **57**, 830-842 (2010).

[16] Brevik, I. & Ellingsen, S. Â. Detection of the Abraham force with a succession of short optical pulses. *Phys. Rev. A* **86**, 025801 (2012).

[17] Ellingsen, S. Â. & Brevik, I. Electrostrictive fluid pressure from a laser beam. *Phys. Fluids* **23**, 096101 (2011).

[18] Gordon, J. P. Radiation forces and momenta in dielectric media. *Phys. Rev. A* **8**, 14-21 (1973).

[19] Chraïbi, H., Lasseux, D., Arquis, E., Wunenburger, R. & Delville, J. Simulation of an optically induced asymmetric deformation of a liquid-liquid interface. *Eur. J. Mech. B* **27**, 419-432 (2008).

[20] Taylor, L. & Alghader, Jo. Monitoring and analysis of thermal deformation waves with a high-speed phase measurement system. *Appl. Opt.* **54**, 9010-9016 (2015).

[21] Malacarne, L. C. *et al.* Nanoscale surface displacement detection in high absorbing solids by time-resolved thermal mirror. *Appl. Phys. Lett.* **92**, 0-3 (2008).

[22] Lukasievicz, G. V. B. *et al.* Pulsed-laser time-resolved thermal mirror technique in low-absorbance homogeneous linear elastic materials. *Appl. Spectrosc.* **67**, 1111-1116 (2013).

[23] Capeloto, O. A. *et al.*. Pulsed photothermal mirror technique: characterization of opaque materials. *Appl Opt* **53**, 7985-7991 (2014).

[24] Astrath, N. G. C., Lukasievicz, G. V. B., Malacarne, L. C. & Bialkowski, S. E. Surface deformation effects induced by radiation pressure and electrostriction forces in dielectric solids. *Appl. Phys. Lett.* **102**, (2013).

[25] Požar, T. & Možina, J. in Fundamentals of Picoscience (ed. Sattle, K. D.) 553-577 (Taylor and Francis, 2013).

[26] Bennis, G. L., Vyas, R., Gupta, R., Ang, S. & Brown, W. D. Thermal diffusivity measurement of solid materials by the pulsed photothermal displacement technique. *J. Appl. Phys.* **84**, 3602 (1998).

[27] Cheng, J. C., Wu, L. & Zhang, S. Y. Thermoelastic response of pulsed photothermal deformation of thin plates. *J. Appl. Phys.* **76**, 716-722 (1994).

[28] Astrath, N. G. C., Malacarne, L. C., Baesso, M. L., Lukasievicz, G. V. B. & Bialkowski, S. E. Unravelling the effects of radiation forces in water. *Nat. Commun.* **5**, 4363 (2014).

[29] Aki, K. & Richards, P. G. Quantitative seismology. (2002).

[30] Galdi, G.P. An Introduction to the Mathematical Theory of the Navier-Stokes Equations: Steady-State Problems. *Springer Monographs in Mathematics*, Sppringer New York, (2011).

[31] Rayleigh, Lord. On waves propagated along the plane surface of an elastic solid. *Proceedings of the London Mathematical Society*, **s1-17**, 1, 4-11, (1885).

[32] Lamb, H. I. On the propagation of Tremors over the Surface of an Elastic Solid. *Philosophical Transactions of the Royal Society of London. Series A*, (1903).

[33] Danilovskaya, V. I. Thermal Stresses in an Elastic Half-Space Arising After a Sudden Heating of Its Boundary. (in Russian) *Prikl. Mat. Mekh* **14** 316-318 (1950)

[34] Danilovskaya, V. I. On a Dynamical Problem of Thermo-Elasticity. (in Russian) *Prikl. Mat. Mekh* **16** 341 (1952)

[35] Michaels, J. E. Thermally induced elastic waves propagation in slender bars. *Proc. 3rd US Nat. Con. Appl. Mech., ASMB, New York* 209 (1958)

[36] Boley, B. A. & Tolins, I. S. Transient Coupled Thermoelastic Boundary Value Problems in the Half-Space. *J. Appl. Mech.* 637-646 (1962).

[37] White, R. M. Generation of elastic waves by transient surface heating. *J. Appl. Phys.* **34**, 3559-3567 (1963)

[38] Scruby, C. B., Dewhurst, R. J., Hutchins, D. A. & Palmer, S. B. Quantitative studies of thermally generated elastic waves in laser-irradiated metals. *J. Appl. Phys.* **51**, 6210-6216 (1980).

[39] Rose, L. R. F. Point-source representation for laser-generated ultrasound. *J. Acoust. Soc. Am.* **75**, 723-732 (1984).

[40] Nowacki, W. Thermoelasticity. (Addison-Wesley Publishing Company, 1962).

[41] Monchalin, J. P. Optical Detection of Ultrasound. *IEEE Trans. Ultrason. Ferroelectr. Freq. Control* **33**, 485-499 (1986).

[42] Aussel, J. D., Le Brun, A. & Baboux, J. C. Generating acoustic waves by laser: theoretical and experimental study of the emission source. *Ultrasonics* **26**, 245-255 (1988).

[43] Goruk, W. S., Vela, P. J. & Stegeman, G. I. Optical Probing Measurements of Surface Wave Generation and Reflection in Interdigital Transducers on LiNbO3. *IEEE Trans. Sonics Ultrason.* **27**, 341-354 (1980).

[44] Draeger, C., Cassereau, D. & Fink, M. Acoustic time reversal with mode conversion at a solid-fluid interface. *Appl. Phys. Lett.* **72**, 1567-1569 (1998).

[45] Royer, D. & Chenu, C. Experimental and theoretical waveforms of Rayleigh waves generated by a thermoelastic laser line source. *Ultrasonics* **38**, 891-895 (2000).

[46] Graebner, J. E., Labs, B., Technologies, L. & Hill, M. Optical Scanning Interferometer for Dynamic. *Ultrasonics* 733-736 (2000).

[47] Hashimoto, K. Y. *et al.* A laser probe based on a sagnac interferometer with fast mechanical scan for RF surface and bulk acoustic wave devices. *IEEE Trans. Ultrason. Ferroelectr. Freq. Control* **58**, 187-194 (2011).

[48] Engan, H. Phase Sensitive Laser Probe for High-Frequency Surface Acoustic Wave Measurements. *IEEE Trans. Sonics Ultrason.* **25**, 372-377 (1978).

[49] Adler, R., Korpel, A. & Desmares, P. An Instrument for Making Surface Waves Visible. *IEEE Trans. Sonics Ultrason.* **15**, 157-161 (1968).

[50] Kavalerov, V., Kasaya, N., Inoue, M. & Fujii, T. Optical probing of nonlinear SAW waveform. *1996 IEEE Ultrason. Symp. Proc.* **2**, 839-844 (1996).

[51] Rooth, S., Bardal, S., Viken, T., Johansen, Øystein & Halvorsen, E. Laserprobe Measurements of SAWs at 3 GHz on a Free Surface of Rotated Y-Cut Quartz. *IEEE Ultrason. Symp.* 201-205 (2001).

[52] Kamizuma, H., Hashimoto, K. Y., Omori, T. & Yamaguchi, M. Development of fast-scanning laser probe system based on knife-edge method for diagnosis of RF surface acoustic wave devices. *Proc. - IEEE Ultrason. Symp.* **3**, 1604-1609 (2005).

[53] Hashimoto, K. Y., Kamizuma, H., Watanabe, M., Omori, T. & Yamaguchi, M. Wavenumber domain analysis of two-dimensional SAW images captured by phase-sensitive laser probe system. *Proc. - IEEE Ultrason. Symp.* **1**, 367-370 (2007).

[54] Landau, L. D., Pitaevskii, L. P., Kosevich, A. M. & Lifshitz, E. M. Theory of Elasticity. (Elsevier Science, 2012).

[55] Lai, C. G. & Wilmanski, K. Surface Waves in Geomechanics: Direct and Inverse Modelling for Soils and Rocks. (Springer Vienna, 2007).

[56] Achenbach, J. D. Wave propagation in elastic solids. (Elsevier Science Publishers B. V., 1973).

[57] Butkov, E. Mathematical Physics. (Addison-Wesley, 1973).

[58] Goodier, J. N. & Bishop, R. E. D. A note on critical reflections of elastic waves at free surfaces. *J. Appl. Phys.* **23**, 124-126 (1952).

[59] Sato, F. *et al.* Time-resolved thermal mirror method: A theoretical study. *J. Appl. Phys.* **104**, 0-9 (2008).

[60] Astrath, F. B. G. *et al.* Time-resolved thermal mirror technique with top-hat cw laser excitation. *Opt. Express* **16**, 12214-12219 (2008).

[61] Astrath, N. G. C. *et al.* Top-hat cw laser induced thermal mirror: A complete model for material characterization. *Appl. Phys. B Lasers Opt.* **94**, 473-481 (2009).

[62] Belancon, M. P. *et al.* Thermal mirror and thermal lens techniques for semitransparent material characterization. *J. Phys. Conf. Ser.* **214**, 012016 (2010).

[63] Astrath, N. G. C. *et al.* Finite-size effect on the surface deformation thermal mirror method. *J. Opt. Soc. Am. B* **28**, 1735 (2011).

[64] Malacarne, L. C. *et al.* Time-resolved thermal lens and thermal mirror spectroscopy with sample-fluid heat coupling: A complete model for material characterization. *Appl. Spectrosc.* **65**, 99-105 (2011).

[65] Bianchi, G. S. *et al.* Resonant excited state absorption and relaxation mechanisms in Tb^{3+}-doped calcium aluminosilicate glasses: an investigation by thermal mirror spectroscopy. *Opt. Lett.* **38**, 4667-4670 (2013).

[66] Zanuto, V. S. *et al.* Thermal mirror spectrometry: An experimental investigation of optical glasses. *Opt. Mater. (Amst).* **35**, 1129-1133 (2013).

[67] Pezarini, R. R. *et al.* On the use of photothermal techniques to study NiTi phase transitions. *Mater. Res. Express* **1**, 026502 (2014).

[68] Zanuto, V. S. *et al.*. Application of photoreactive barium titanate (BaTiO3) beam fanning to the Photothermal mirror technique: An experimental analysis. *Appl. Spectrosc.* **69**, 794-801 (2015).

[69] Aréstegui, O. S. *et al.* Combined photothermal lens and photothermal mirror characterization of polymers. *Appl. Spectrosc.* **68**, 777-783 (2015).

[70] Souza, S. T. *et al.* Direct measurement of photo-induced nanoscale surface displacement in solids using atomic force microscopy. *Opt. Mater. (Amst).* **48**, 71-74 (2015).

[71] Royer, D. & Dieulesaint, E. Elastic waves in solids. Springer (Springer-Verlag Berlin Heidelberg, 2000).

[72] Shen, J., Lowe, R. D. & Snook, R. D. A model for cw laser induced mode-mismatched dual-beam thermal lens spectrometry. *Chem. Phys.* **165**, 385-396 (1992).

[73] ASM International Handbook, V. 2. Properties and selection: Nonferrous alloys and special-purpose materials. ASM Metals Handbook 2, (1990).

[74] Lamb, H. I. On waves in an elastic plate. *Proc. R. Soc. London. Ser. A* **93**, 114 LP-128 (1917).

[75] Maxwell, J. C. *A Treatise on Electricity and Magnetism* (Constable, London, 1891) [reprinted by Dover Books, New York, 1954].

[76] Lebedew, P. Experimental examination of light pressure. *Ann. Phys.* **6**, 433-458 (1901).

[77] Minkowski, H. Die Grundgleichungen für die elektromagnetischen Vorgänge in bewegten. *Nachr. Königl. Ges. Wiss. Göettingen*, 53-111 (1908).

[78] Abraham, M. Zur Elektrodynamik bewegter Krper. Rend. Circ. Mat. Palermo. *Rend. Circ. Mat. Palermo* **28**, 1-28 (1909).

[79] Jones, R. V. & Leslie, B. The measurement of optical radiation pressure in dispersive media. *Proc. R. Soc. London Ser. A* **360**, 347-363 (1978).

[80] Ashkin, A. & Dziedzic, J. M. Radiation pressure on a free liquid surface. *Phys. Rev. Lett.* **30**, 139-142 (1973).

[81] Loudon, R. Radiation pressure and momentum in dielectrics. *Fortschr. Phys.* **52**, 1134-1140 (2004).

[82] Walker, G. B., Lahoz, D. G. & Walker, G. Measurement of the Abraham force in a barium titanate specimen. *Can. J. Phys.* **53**, 2577-2586 (1975).

[83] Zhang, L., She, W., Peng, N. & Leonhardt, U. Experimental evidence for Abraham pressure of light,*New J. Phys.* **17**, 053035 (2015).

[84] Landau, L. D. & Lifshitz, E. M. *Electrodynamics of continuous media* (Pergamon Press, New York, 1984).

[85] Brevik, I. Experiments in phenomenological electrodynamics and the electromagnetic energy-momentum tensor. *Phys. Rep.* **52**, 133-201 (1979).

[86] von Helmholtz, H. *Wied. Ann.* **13**, 385 (1881).

[87] Shevchenko, A. & Hoenders, B. J. Microscopic derivation of electromagnetic force density in magnetic dielectric media. *New J. Phys.* **12**, 053020 (2010).

[88] Khattab, I. S., Bandarkar, F., Fakhree, M. A. A. & Jouyban, A. Density, viscosity, and surface tension of water+ethanol mixtures from 293 to 323K. *Korean J. Chem. Eng.* **29**, 812-817 (2012).

[89] Aminabhavi, T. M. & Gopalakrishna, B. Density, Viscosity, Refractive Index, and Speed of Sound in Aqueous Mixtures of N,N-Dimethylformamide, Dimethyl Sulfoxide, N,N-Dimethylacetamide, Acetonitrile, Ethylene Glycol, Diethylene Glycol, 1,4-Dioxane, Tetrahydrofuran, 2-Methoxyethanol, and 2-Ethoxyethanol at 298.15 K. *J. Chem. Eng. Data* **40**, 856-861 (1995).

[90] Horwitz, C., Fremlin, J. H. & Farr, R. F. Determination of Interfacial Tension of Emulsion Droplets. *Phys. Med. Biol.* **16**, 399-405 (1964).

[91] Azizian, S. & Hemmati, M. Surface tension of binary mixtures of ethanol + ethylene glycol from 20 to 50°C.*J. Chem. Eng. Data* **48**, 662-663 (2003).

[92] Del Mar Graciani, M., Rodríguez, A., Muñoz, M. & Moyá, M. L. Micellar solutions of sulfobetaine surfactants in water-ethylene glycol mixtures: Surface tension, fluorescence, spectroscopic, conductometric, kinetic studies. *Langmuir* **21**, 7161-7169 (2005).

[93] Bohne, D., Fischer, S. & Obermeier, E. Thermal, Conductivity, Density, Viscosity, and Prandtl-Numbers of Ethylene Glycol-Water Mixtures. *Berichte der Bunsengesellschaft für Phys. Chemie* **88**, 739-742 (1984).

[94] Kedenburg, S., Vieweg, M., Gissibl, T. & Giessen, H. Linear refractive index and absorption measurements of nonlinear optical liquids in the visible and near-infrared spectral region. *Opt. Mater. Express* **2**, 1588 (2012).

[95] El-Kashef, H. The necessary requirements imposed on polar dielectric laser dye solvents - II.*Phys. B Condens. Matter* **311**, 376-379 (2002).

[96] Arnaud, N. & Georges, J. On the analytical use of the Soret-enhanced thermal lens signal in aqueous solutions.*Anal. Chim. Acta* **445**, 239-244 (2001).

[97] Sakai, K., Mizuno, D. & Takagi, K. Measurement of liquid surface properties by laser-induced surface deformation spectroscopy. *Phys. Rev. E* **63**, 046302 (2001).

[98] Kim, K.-Y. *et al.* Terahertz emission from ultrafast ionizing air in symmetry-broken laser fields. *Opt. Express* **15**, 4577 (2007).

[99] Herculano, L. S. *et al.* Investigation of the photobleaching process of eosin y in aqueous solution by thermal lens spectroscopy. *J. Phys. Chem. B* **117**, 1932-1937 (2013).

[100] Bethune-Waddell, M. & Chau, K. J. Simulations of radiation pressure experiments narrow down the energy and momentum of light in matter. *Reports Prog. Phys.* **78**, 122401 (2015).

[101] Požar, T. *et al.* Isolated detection of elastic waves driven by the momentum of light. *Nat. Commun.* bf 9, 3340 (2018).

[102] Zanuto, V. S. Pressão de radiação: Sobre os efeitos das forças de radiação em água. (2015).